# CHAPTER 4

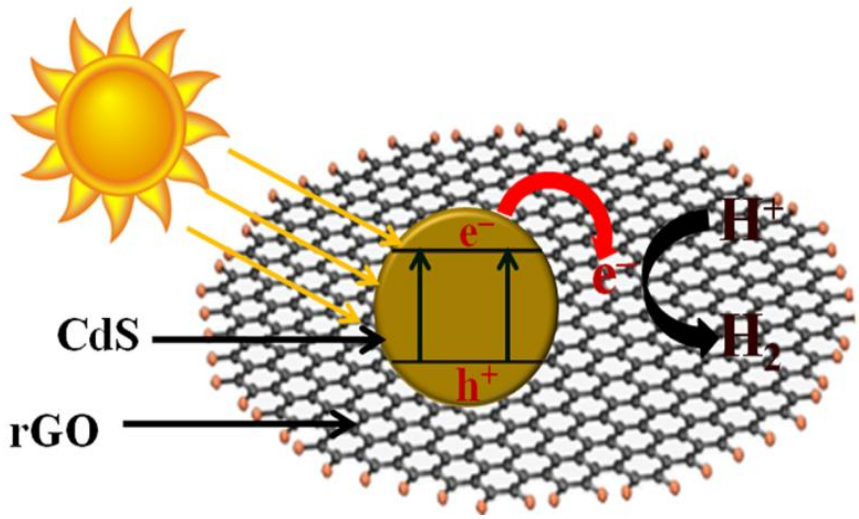

4

# Chapter

# Results and discussion

Contents

## 4.1 Photocatalytic activity

The activities of all catalysts in mL of $H_2$ produced at NTP for 2 h of irradiation is given in Table 4.1. The reported values are average of number of repeated runs. It is order to mention that no hydrogen production was observed either in the absence of irradiation or without photocatalyst. Therefore, it was concluded that the hydrogen was produced by photocatalysis of water. Since, the electrolyte contained $S^{2-}$and $SO_3^{2-}$, the overall reaction is represented as given below:

$$H_2O + S^{2-} + SO_3^{2-} \xrightarrow{h\nu} H_2 + 2OH^- + S_2O_3^{2-} \quad (4.1)$$

(Elementary steps of the reaction are discussed in the section 4.15 under the heading of kinetics and mechanism).

**Table 4.1:** Activity of photocatalysts.

| Catalysts | Hydrogen evolved in 2 h mL.(g-CdS)$^{-1}$ at NTP |
|---|---|
| 1 | 1.6 (±0.2) |
| 2 | 9.6 (±0.2) |
| 3 | 14.6 (±0.2) |
| 4 | 10.8 (±0.2) |
| 5 | 6.0 (±0.2) |
| 6 | 9.0 (±0.2) |

It is observed from the Table 4.1 that the activity of unsupported catalyst CdS was low (catalyst–1). Since, it was an unsupported CdS therefore, as

discussed in the earlier sections [130–133], the photo-generated electrons-holes could not be effectively prevented from recombination and hence a low activity.

It is further observed that the activity of CdS is improved significantly by mixing it physically with GO/rGO (5 & 6). This observation is attributed to the fact that the presence of GO/rGO results into a better charge separation and a greater mobility of charges to the surface [also discuss in section 4.5].

The Table 4.1 also shows that catalyst–3 had a superior activity compared to catalyst–2. Catalyst–3 was CdS supported on rGO whereas catalyst–2 was CdS supported on GO. The preparation technique was same for both the catalysts. The higher activity of catalyst–3 compared to that of catalyst–2 is attributed to high electronic conductivity of rGO compared to GO. The structure of the GO has the various oxygen containing groups such as carboxyl, hydroxyl or epoxy groups with network of $sp^2$-hybridized –C–C– atoms and significant amount of $sp^3$ C–O bonds. However, after an efficient reduction, rGO doesn't have such oxygenated groups [discussed in FTIR studies section 4.2]. Presence of these polar oxygen units results into a very substantial decrease in conductivity in GO [290]. A better conductivity would facilitate efficient transfer of electrons and thus restrict the recombination. A remarkable observation is that catalyst prepared by hydrothermal technique (catalyst–4) had a lower activity compared to catalyst-3 which had same composition but prepared by a gas-solid reaction. It is in order to mention that the hydrothermal technique is a most preferred technique reported in the literature [201–209] for preparation of CdS supported on graphene.

It should also be mentioned that, in earlier works in our laboratory [168,280], CdS supported on alumina was prepared by the same technique as in the present study, i.e. impregnation and then reacting $CdSO_4$ with $H_2S$ gas at 573 K. The better activity of the catalyst was attributed to the fact that the resulting CdS had a non-stoichiometric composition with sulphur deficiency. The sulphur deficiency made the CdS to behave like an *n*-type semiconductivity. Therefore, it is likely that preparation of catalyst–2 and 3 by impregnation of GO and rGO, respectively and reacting with $H_2S$ gas at an elevated temperature has resulted into formation of *n*-type CdS. The GO/rGO has *p*-type semiconductivity [291,292]. Hence formation of a *p*-*n* junction with *p*-type GO/rGO is likely. It has been already discussed in section 2.6 that, the creation of heterojunction is one of the most efficient way among all available strategies to separate photogenerated charges resulting in the improvement of photocatalytic activity for photocatalytic hydrogen production.

It has been described below that a chemical interaction does exist between S of CdS and C of GO/rGO when catalysts were prepared by gas-solid reaction. Such chemical interaction was observed to be very insignificant in the catalyst prepared by hydrothermal technique. Therefore, we attribute the highest activity of catalyst–3 due to the existence of a chemical interaction at the interface of CdS and rGO. Such an interface might have resulted into the formation of a *p*-*n* junction as well.

## 4.2 FTIR studies

Formation of functional groups during the catalysts preparation was analyzed by FTIR as shown in Fig.4.1 & 4.2. Fig. 4.1 shows the FTIR spectra of graphite, GO and rGO. Two peaks were observed in the spectrum of graphite [Fig. 4.1A] at 1590 and 1220 $cm^{-1}$ which are assigned to C=C bond and C-OH. Chemical and structural changes of graphite upon oxidation are reflected in GO spectrum, as shown in [Fig 4.1B]. A broad band around 3400 $cm^{-1}$ signifies stretching vibration of surface hydroxyls (~ 3400 $cm^{-1}$) and water absorption (~3200 $cm^{-1}$).The peaks located at ~1740 $cm^{-1}$ (C=O stretching) are from carbonyl. Melucci et al. [293] & Chen et al. [294] also reported that peak at 1732 $cm^{-1}$ in GO attributed to the stretching vibration of a carbonyl. The peak observed at 1630 $cm^{-1}$ is related to the in-plane vibrations of $sp^2$- hybridized C−C bonding or the H−O−H bending band of the adsorbed $H_2O$ molecules. Mondal et al [295] also reported such type of assignment for GO. They reported peak at 1626 $cm^{-1}$ attributed to $sp^2$-hybridized C−C bonding or the H−O−H bending band of the adsorbed $H_2O$ molecules. Peak observed at ~1209 $cm^{-1}$ is due to carboxylic groups (C−OH stretching) from carboxylic groups and at ~1065 $cm^{-1}$ (skeletal C−O) peak from carbonyl, carboxylic and epoxy groups. Xu et al. [296] also reported same type of assignment of peak at 1057 $cm^{-1}$. This peak is attributed to a C–O in C–OH or C–O–C functional groups with ignoring the possible weak contributions from carboxyls & ketones. Moreover, an absorption peak is observed at 867 $cm^{-1}$ assigned to the symmetric stretching of epoxy groups [297].

The presence of these oxygen-containing groups reveals that the graphite has been oxidized. The whole spectrum of FTIR spectra of GO/rGO is given in Table 4.2.

**Table 4.2:** The whole spectrum of FTIR spectra of GO/rGO observed by FTIR

| | GO | rGO | Ref. |
|---|---|---|---|
| C–H, out of Plane vag | 867 | - | *297 (a)* |
| C–O | 1065 | - | *296* |
| C–OH of alcohol | 1209 | 1224 | *293* |
| C=C of carboxylic acid | 1630 | - | *295* |
| C=O of carbonyl groups | 1739 | 1747 | *293, 294* |
| C=O stretch | 2178 | | *297 (b)* |
| -$CO_2$ | 2362 | | *297 (b)* |
| –OH group | 3275 | 3018 | *295* |

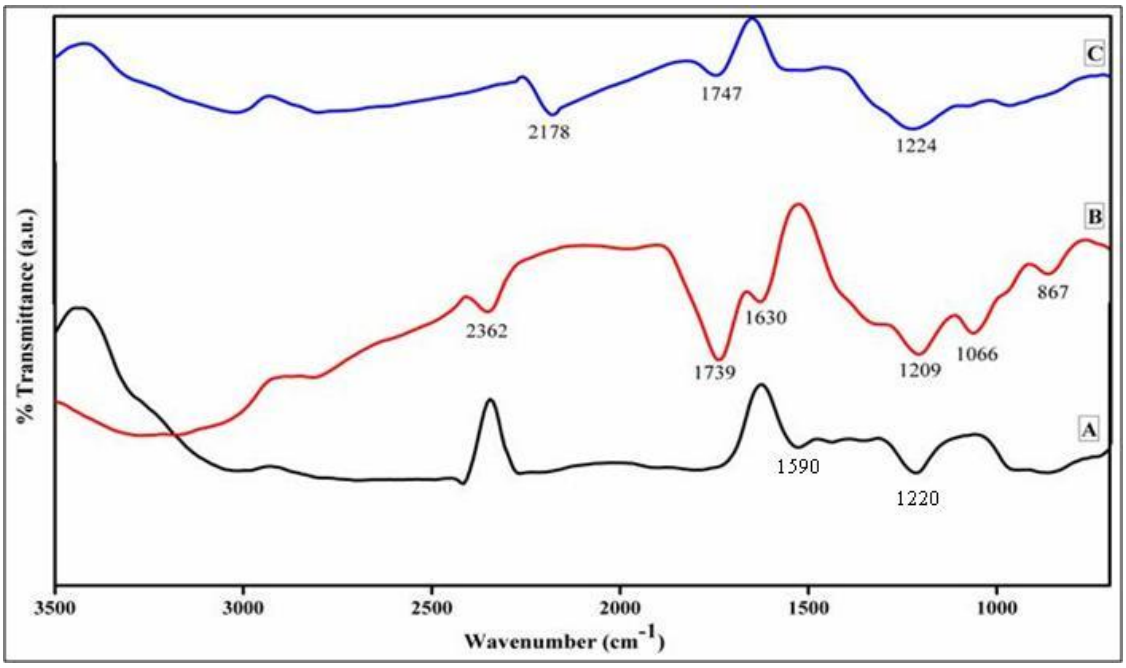


**Figure 4.1:** FTIR comparison of graphite (A), graphite oxide (B), reduced graphite oxide (C).

Reduction of GO was carried out done by reacting with Zn dust in acidic medium where following reaction did take place:

$$GO + Zn + H_2O \rightarrow GO + Zn^{2+} + 2e^- + H^+ + OH^- \rightarrow rGO + ZnO + H_2O \qquad (4.2)$$

As expected several oxygen containing functional groups present in GO were either not observed or their intensity was diminished in rGO. FTIR peaks of reduced graphite oxide are shown in Fig. 4.1C. Much lower absorption intensity for the peak at 1747 $cm^{-1}$ peak and skeletal C−O (1065 $cm^{-1}$) has disappeared. This result confirms the reduction of GO to rGO.

The FTIR spectra of photocatalysts are shown in Fig. 4.2. The presence of oxygenated functional groups similar to GO and rGO is observed. A comparison reveals (catalyst–3 & 4) that peak intensity of skeletal C−O (1065 $cm^{-1}$) (not shown in the Fig. 4.2) and C=O of carbonyl groups (1739 $cm^{-1}$) are diminished.

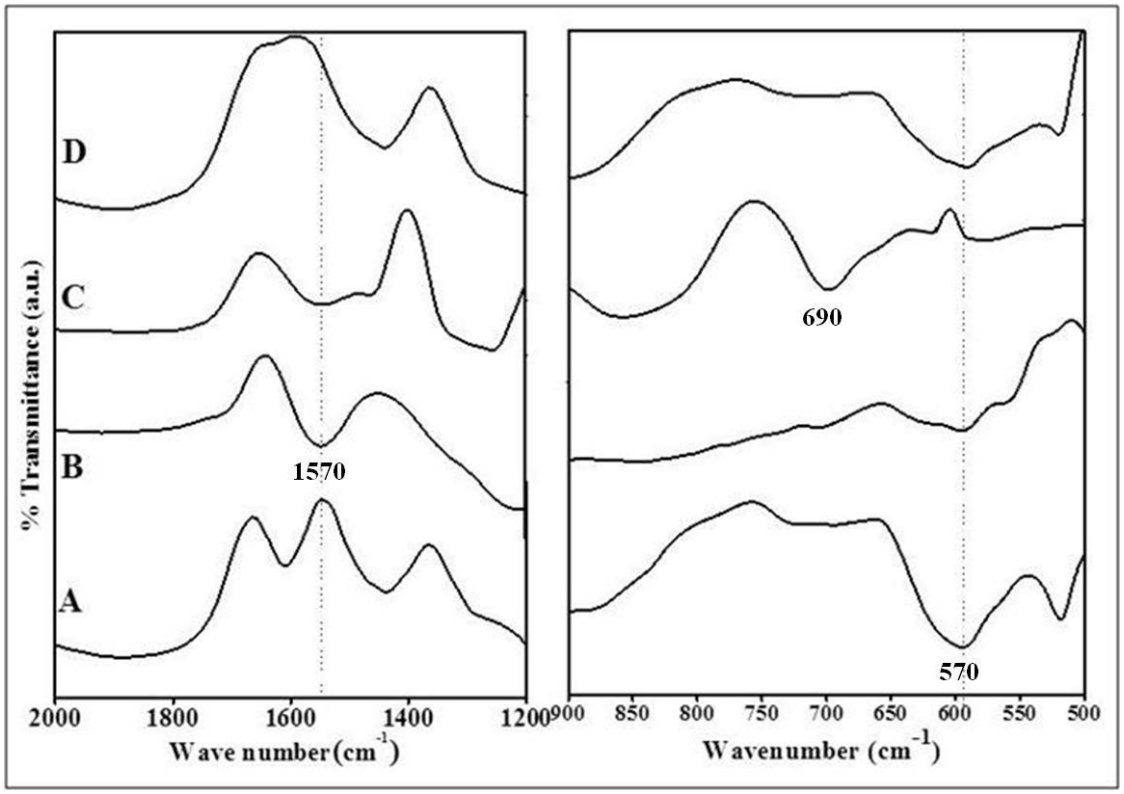


**Figure 4.2**: FTIR comparison of catalyst–1 (A), catalyst–2 (B), catalyst–3 (C), and catalyst–4 (D).

The absorption peak at ~570 $cm^{-1}$ in catalyst–1 (unsupported CdS) is assigned to the stretching vibration of Cd–S [298,299]. This peak is also observed in catalysts–2 and 4. A remarkable observation is the appearance of a strong absorption peak at ~690 $cm^{-1}$ in catalyst–3. This peak is not observed in any other catalyst. We assign this peak also to the stretching vibration of Cd–S, which is red shifted in comparison to the peak in pure CdS at 570 $cm^{-1}$. Coupling of vibrations is a common phenomenon which causes shift in peak positions. In our case, we attribute the shift to the coupling of Cd–S and C–S vibrations. Such a coupling provides an indication of chemical interaction between CdS and graphene oxide in catalyst–3. Yogamalkar et al. [300] have also reported shift in Cd–S stretching peak position to 671 $cm^{-1}$ in CdS–graphene oxide system. They have attributed this shift to inclusion of CdS nanoparticles in the GO matrix. The shift in peak position from 570 $cm^{-1}$ (catalyst–1, 2 & 4) to 690 $cm^{-1}$ (catalyst–3) has been assigned to a change in the bond strength of Cd–S in catalyst–3 due to CdS being surrounded by rGO and resulting into a chemical interaction between CdS and rGO. It should also be noted that this catalyst showed highest activity towards photocatalytic decomposition of water.

Another significant observation is appearance of absorption peaks at ~1550 $cm^{-1}$ in catalyst–2 and 3 which were CdS supported on GO/rGO and prepared by gas-solid reaction as described above. The literature [297,301] reports C–S stretching frequency at ~1570 $cm^{-1}$. Earlier workers have also reported likelihood of electronic interactions between C and S through $\pi^*$ orbital of GO/rGO and *n*-orbital of S of CdS [199,302–304]. It is further observed this absorption peak is not seen in catalyst–4 (prepared by hydrothermal technique). The FTIR study gives an indication of interaction as discussed above in catalyst–2 and 3. The

absorption band may also appear because of doping of sulphur in GO/rGO. Since during the preparation of catalyst–2 and 3, $H_2S$ gas was passed at high temperature, such doping is likely. Therefore, it is concluded that an interfacial electronic interaction between CdS and GO/rGO or doping of GO/rGO with sulphur has taken place in catalyst–2 & 3, and phenomenon is largely absent in catalyst–4.

### 4.3 XRD studies

Fig. 4.3 shows the XRD patterns of graphite, GO and rGO. Characteristic peaks of crystalline graphite at 2θ, 26.54$^o$, 44.47$^o$, 54.66$^o$ and 77.54$^o$corresponding to (002), (101), (004), and (112) planes, respectively are seen in Fig. 4.3A. The analysis of (002) peak of graphite gives an inter-planar spacing of 0.335 nm. The XRD patterns of GO [Fig. 4.3B] and rGO [Fig. 4.3C] are in line with those reported in the literature [305,306]. An intense and sharp peak centred at 2θ=10.25° of (001) plane which corresponds to an inter-planar spacing of 0.86 nm was observed in GO. The larger interlayer spacing of GO compared to that of graphite is due to the formation of oxygen-containing functional groups [307].

In case of rGO [Fig. 4.4C], a small characteristic diffraction peak of graphite oxide of plane (001) at approximately 10.68$^o$ is also observed. It indicates that reduction of GO by Zn dust in acidic medium was not completed and a few oxygen-containing functional groups still existed in the sample. A broad diffraction peak of (002) plane of rGO at about 2θ=24$^o$ is also seen. The broadening and shift of the characteristic diffraction peak of graphite from

$26.54^{o}$ to $24^{o}$ is due to the short-range order in stacks of layers in rGO. The interlayer spacing of rGO was 0.37 nm, slightly larger than that of graphite.

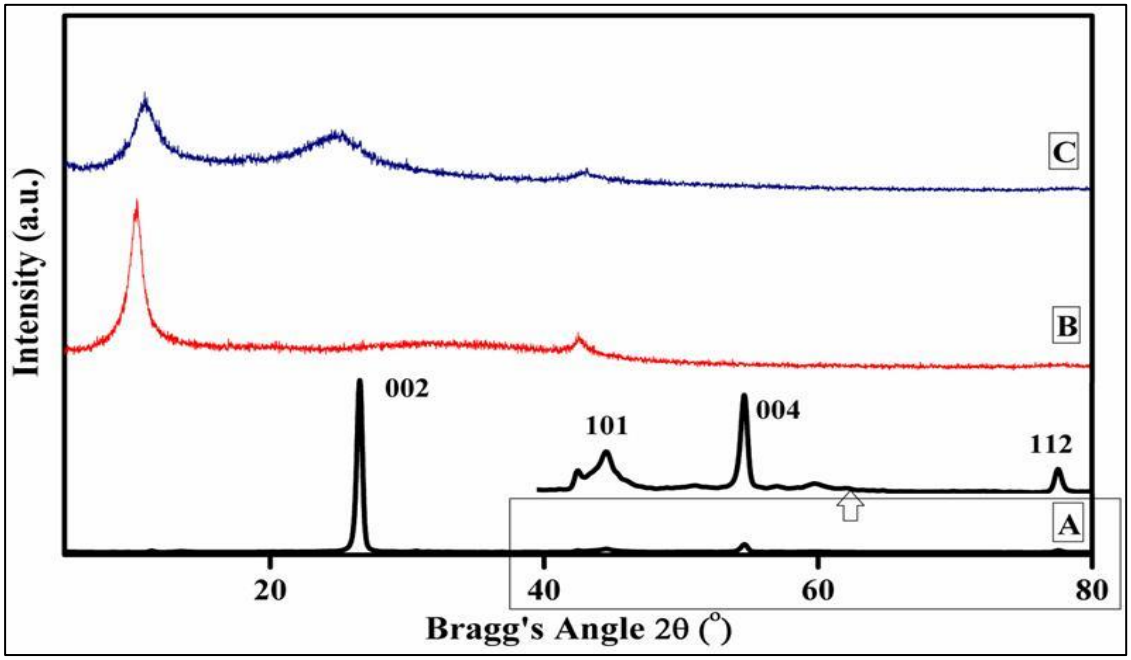


**Figure 4.3:** XRD pattern of sample graphite (A), GO (B), rGO (C).

The enlargement in spacing may be due to presence of residual oxygen-containing functional groups or other structural defects. Fu et al. [308] reported preparation of graphene by Hummers method and then reduction by hydrothermal method and stated that the broadening and shift of the characteristic diffraction peak of graphite due to the short-range order in stacked stacks. Gao et al. [309] also stated rGO had a higher interlayer spacing compared to graphite due to oxygen-containing functional groups or other structural defects.

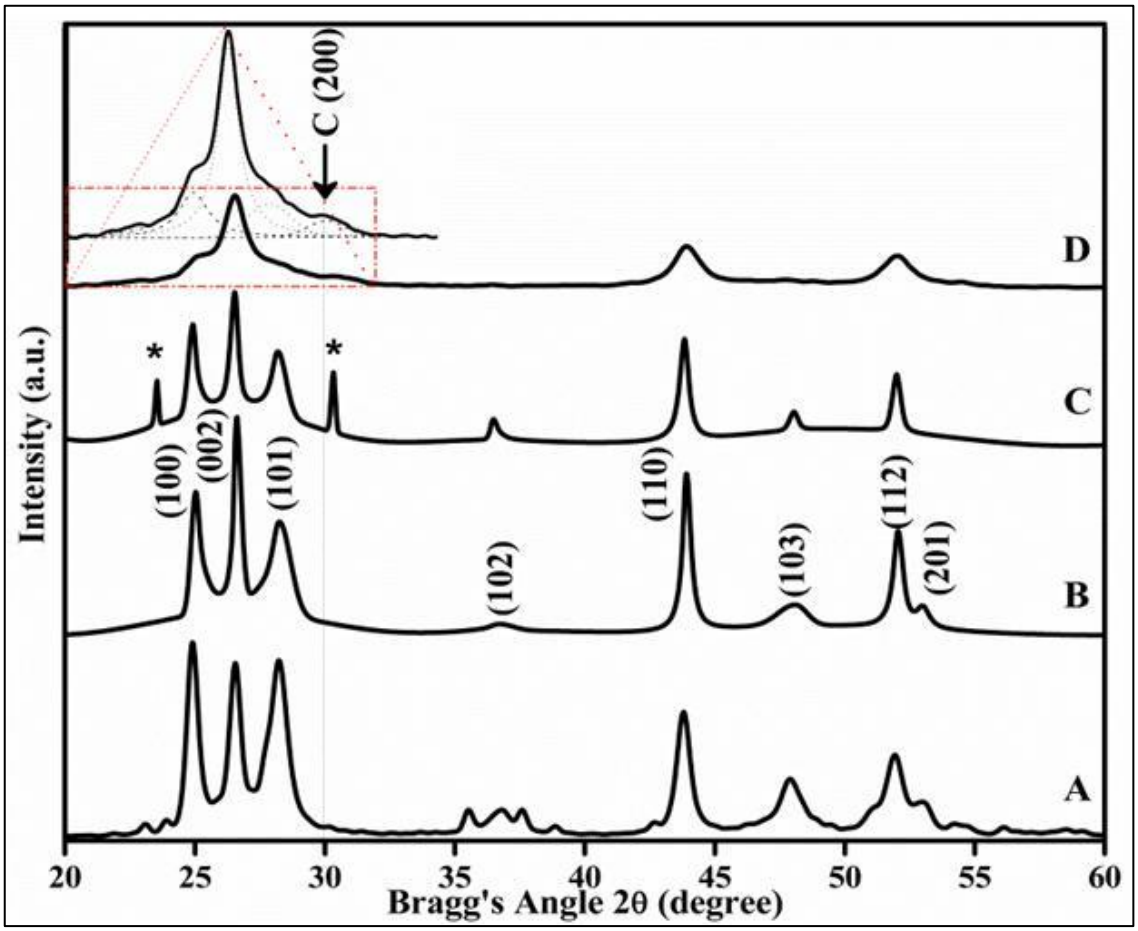


**Figure 4.4:** XRD pattern of catalysts: catalyst–1 (A), catalyst–2 (B), catalyst–3 (C) and catalyst–4 (D).

Fig. 4.4 shows the XRD pattern of catalyst–1 to 4. The peak positions were located and the d values were calculated by applying Bragg's equation and are given in Table 4.3. Standard values of the hexagonal (H) and cubic (C) phases of CdS are also given. A comparison of calculated d values with the standard data shows that all the peaks observed in catalysts–1 to 3 correspond to cadmium sulphide with hcp structure. The characteristic peak of the cubic phase at d=2.91 Å [310] is not observed in these samples. These catalysts were prepared by a gas-solid reaction as described earlier. While in catalyst–4 which was prepared by hydrothermal method, the characteristic peak of cubic phase of CdS at 2.90 Å is also observed.

**Table 4.3:** d-values by XRD analysis

| **Standard values of d and miller indices** | | | | **Experimental values of d** | | | |
|---|---|---|---|---|---|---|---|
| **Hexagonal** | | **Cubic** | | | | | |
| **Miller Indices** | **Hexagonal Phase** | **Miller Indices** | **Cubic Phase** | | | | |
| hkl | d(Å) | hkl | d(Å) | Catalyst 1 | Catalyst 2 | Catalyst 3 | Catalyst 4 |
| 100 | 3.58 | - | - | 3.56 | 3.58 | 3.57 | 3.54 |
| 002 | 3.36 | 111 | 3.36 | 3.35 | 3.36 | 3.35 | 3.37 |
| 101 | 3.16 | - | - | 3.16 | 3.17 | 3.16 | 3.14 |
| 102 | 2.45 | - | - | 2.43 | 2.44 | 2.46 | - |
| - | - | 200 | 2.91 | - | - | - | 2.90* |
| 110 | 2.06 | 220 | 2.06 | 2.07 | 2.06 | 2.06 | 2.06 |
| 103 | 1.89 | - | - | 1.89 | 1.89 | 1.89 | - |
| 200 | 1.79 | 311 | 1.75 | - | - | - | 1.75 |
| 112 | 1.76 | - | - | 1.75 | 1.76 | 1.75 | - |
| 201 | 1.73 | - | - | 1.72 | 1.72 | - | - |
| 004 | 1.67 | 222 | 1.68 | 1.69 | 1.67 | - | - |
| 203 | 1.39 | 331 | 1.33 | 1.39 | 1.40 | - | - |

Hydrothermal technique resulted in formation of CdS which was mixture of both cubic and hexagonal phases. Sahu et al. [168] have explained that when ammonia was present on the surface during formation (sulphurization stage of catalyst) of CdS, it reduced the ionization of $Cd^{2+}$ ions. This reduction in ionization affected the stacking sequence in CdS crystal and cubic (zinc blend) structure could also form. In absence of ammonia, wurtzite (hcp) structure was

favoured. Actually, in the case of cubic structure of CdS, FCC structure was formed by both the S and Cd ions, individually and therefore the ions of same kind 'see' each other. However, in the case of wurtzite structure, the positions of S ions are hexagonal closed pack. Therefore, the possibility of interaction between atoms of the same kind is lower in the wurtzite structure. Since the ions of same kind do not like to 'see' each other; therefore, greater ionization is more favoured with the wurtzite structure. In our case for catalyst–4, ammonia was present during the formation of CdS (CdS is formed by precipitation in ammoniacal solution followed by a hydrothermal treatment). It reduced the ionization of cadmium sulphate atoms and, therefore cubic (zinc blende) structure was also observed in the catalysts. However, in the case of catalyst–2 and 3, pre-adsorbed ammonia is desorbed from the surface because resulting mass was heated at 573 K [section 3.2], therefore, the possibility of formation of cubic structure reduced. It is also in order to mention that the cubic phase of CdS is reported to have a lower activity [162,228,311]. Zhang et al. [311] has explained the structural characteristics, electronic structures, and chemical bonding of wurtzite and zinc-blende CdS. It has been shown that electronic dipole moment was formed due to the distortion of tetrahedron in wurtzite CdS crystal structures. Therefore, internal electric field was formed, which helped in separation of photogenerated charge-carriers. However, it was totally absent in zinc-blende CdS. They also reported that wurtzite CdS has stronger ionic character and consequently higher charge carrier mobility. Moreover, wurtzite CdS has a low carrier effective mass than those of Zinc blende CdS, which helped in a higher charge mobility, and also suppressed their recombination rate which results into a higher photocatalytic activity of wurtzite compared to zinc blend CdS.

It should also be noted that two unidentified peaks (marked with *) were also observed in catalyst–3. It may be because of presence of some form of carbon in the sample.

Unit cell parameters '*a*' and '*c*' of the hexagonal CdS were calculated using the formula:

$$\frac{1}{d^2} = \frac{4}{3}\left(\frac{h^2+hk+k^2}{a^2}\right) + \frac{l^2}{c^2} \qquad (4.3)$$

**Table 4.4:** Unit cell parameters and average crystalline size (nm) of catalysts

| Catalysts | Unit cell parameters | | | Mean crystalline size (nm) (~) |
|---|---|---|---|---|
| | a (Å) | c (Å) | c/a | |
| 1 | 4.140 | 6.712 | 1.6213 | 22 |
| 2 | 4.134 | 6.685 | 1.6171 | 29 |
| 3 | 4.129 | 6.718 | 1.6270 | 26 |
| 4 | 4.132 | 6.748 | 1.6320 | 6 |

The d values of (110) and (002) planes were used. The values are shown in Table 4.4. The reported values of a, c, and c/a for CdS are 4.121 Å, 6.682 Å and 1.621, respectively [312]. The calculated values nearly match with the experimental values. The XRD peaks of the catalysts were rather broad; therefore, exact location of peak position may not be very accurate. Hence, on the basis of small variations in lattice parameters, we do not conclude any structural defect in CdS. It is order to mention that in earlier work from our laboratory [281], it has been reported that CdS prepared by the gas-solid reaction (same as in

the present study) showed an *n*-type semiconductivity owing to deficiency in S with respect to stoichiometric composition. In absence of anything in contrary, we assume that CdS present in catalysts–1 to 3 prepared by the gas-solid reaction also have *n*-type semiconductivity.

Mean crystallite sizes were estimated by measuring full width at half intensity of selected peaks. Instrumental broadening was subtracted from the total broadening and the Scherrer equation was used. Since the highest intensity peak of CdS (002) suffered from interference from diffraction pattern of rGO, crystallite sizes were calculated by measuring the broadening of the (110) peaks for all the catalysts. The results are given in Table 4.4. It is seen from the table that the catalyst prepared by hydrothermal technique (catalyst–4) had a much lesser crystallite size (~6 nm) in comparison to those of catalyst–2 and 3 (~29 nm and ~26 nm, respectively). Still, catalyst–3 showed a much better activity compared to catralyst-4. Thus, the crystallite size cannot be taken as sole criteria for a better activity; there are other microstructural properties which may be more responsible for the observed better activity of catalyst prepared by gas-solid reaction (catalyst–3).

### 4.4 TEM and electron diffraction studies (SAED)

The TEM images of catalyst–2, 3 and 4 are shown in Fig. 4.5. CdS particles are seen to be uniformly distributed on graphene. Average particle sizes were also calculated as ~29 nm, 27 nm and 12 nm for catalyst–2, 3 and 4, respectively [Table 4.5]. These particle sizes are almost equal to the crystallite sizes calculation by XRD which were reported above. Hence, agglomeration of crystallites is negligible in all the catalysts.

**Table 4.5:** Average particle size (nm) of CdS by TEM.

| Catalysts | Size (nm) |
|---|---|
| 2 | 29 |
| 3 | 27 |
| 4 | 12 |

Selected area electron diffraction (SAED) patterns for catalyst–2, 3 and 4 are shown in Fig. 4.6. The *d*-spacings were calculated for all these catalysts. For catalyst–2 calculated values match with standard values of the hexagonal phase of CdS, i.e. 3.36 Å, 2.45 Å, 2.06 Å and 1.89 Å corresponding to (002), (102), (110), and (103) planes, respectively. Similarly for catalyst–3 also values matched with the hexagonal phase of CdS 3.36 Å, 2.45 Å, 2.06 Å and 1.89 Å corresponding to (002), (102), (110), and (103) planes, respectively. However, the catalyst–4 shows the presence of both the cubic phase 2.90 Å corresponding to (200), with hexagonal phase 3.36 Å, 2.06 Å and 1.89 Å corresponding to (002), (110), and (103) planes, respectively.

It is in order to mention that the XRD analysis had also revealed that in catalyst–4 both the phases were present. As reported earlier [161,304,305], the cubic phase has a lower activity and therefore, the presence of this phase could be one of the reasons of observed lower activity of catalyst–4 as compared to catalyst–3 which contained only the hexagonal phase of CdS. The lower activity of catalyst–2 with respect to catalyst–4 is attributed to the fact that in the former GO was used whereas in the later rGO, which has a better electrical conductivity.

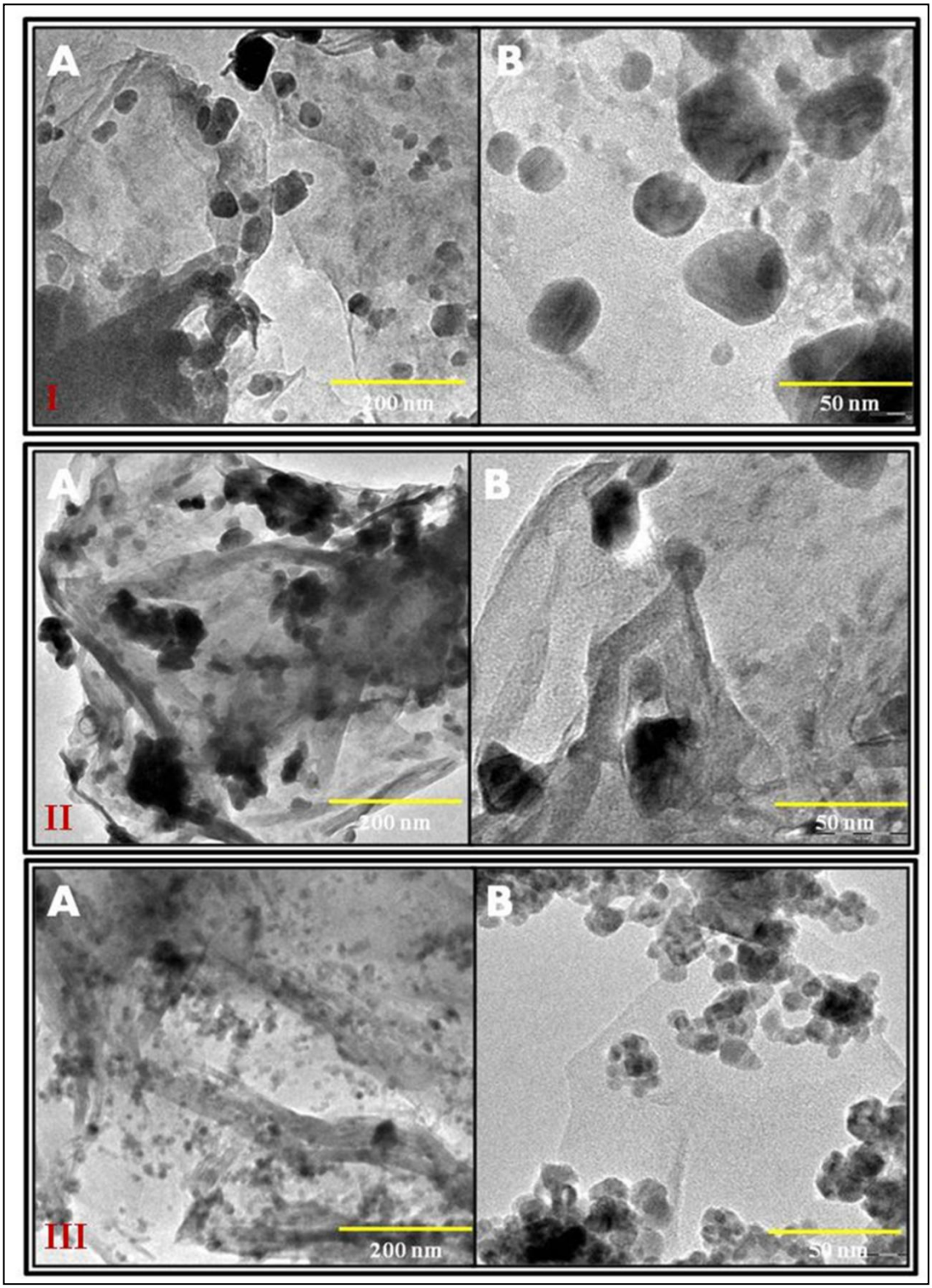


**Figure 4.5:** TEM images of catalyst–2 (I), catalyst–3 (II), and catalyst–4 (III).

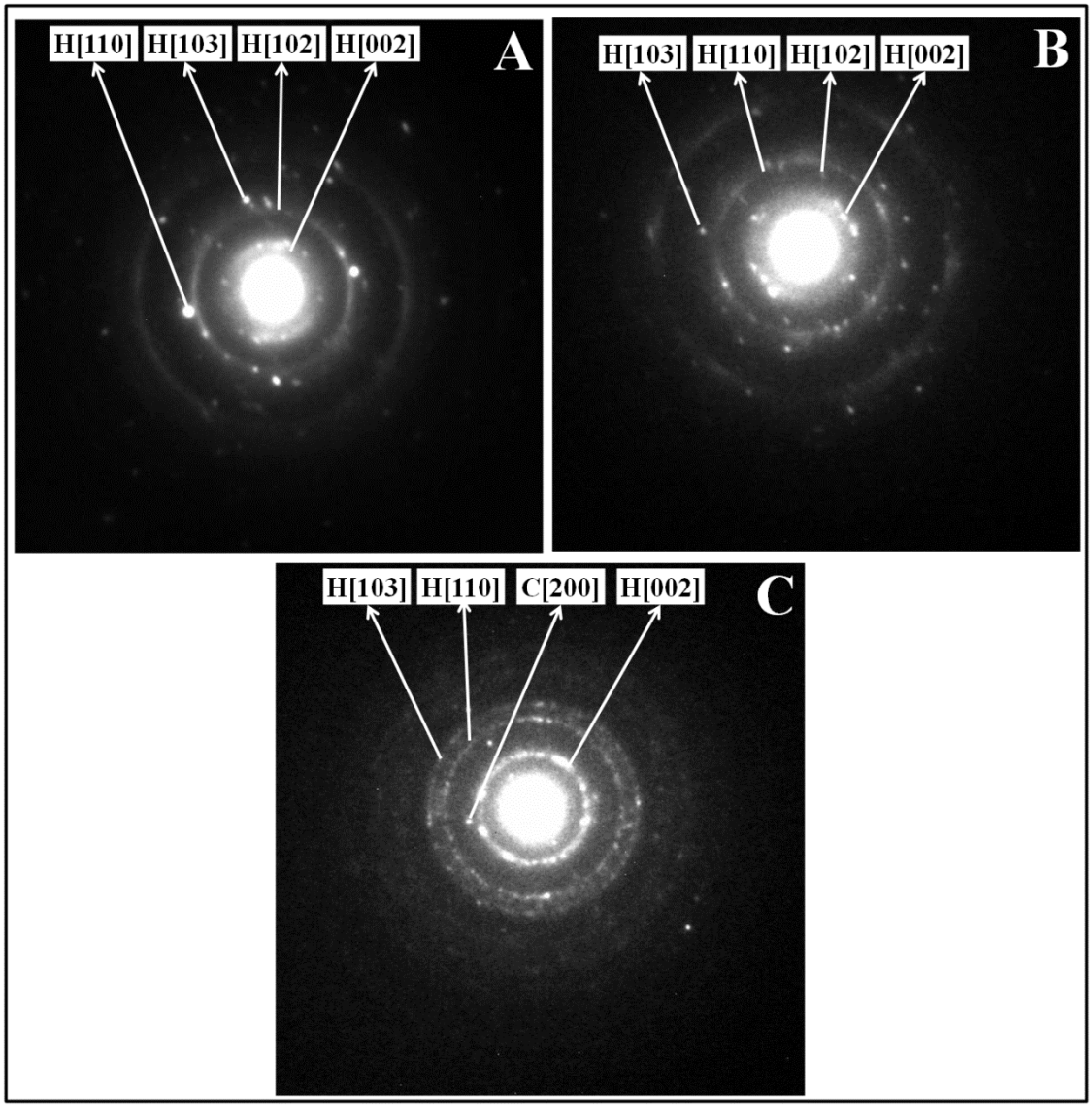


**Figure 4.6:** Selected area diffraction pattern forcatalyst–2 (A), catalyst–3 (B), and catalyst–4 (C).

### 4.5 Photoluminescence studies

Fig. 4.7 shows PL spectra of catalysts–1 to 4 with the excitation wavelength of 200 nm. For the sake of comparison PL of a physical mixture (well mixed in mortar and pestle) of CdS and GO/rGO (denoted as catalyst–5 and 6) was also recorded. Strong emission peaks at about 530 nm (corresponding to 2.4 eV) were observed for all catalysts.

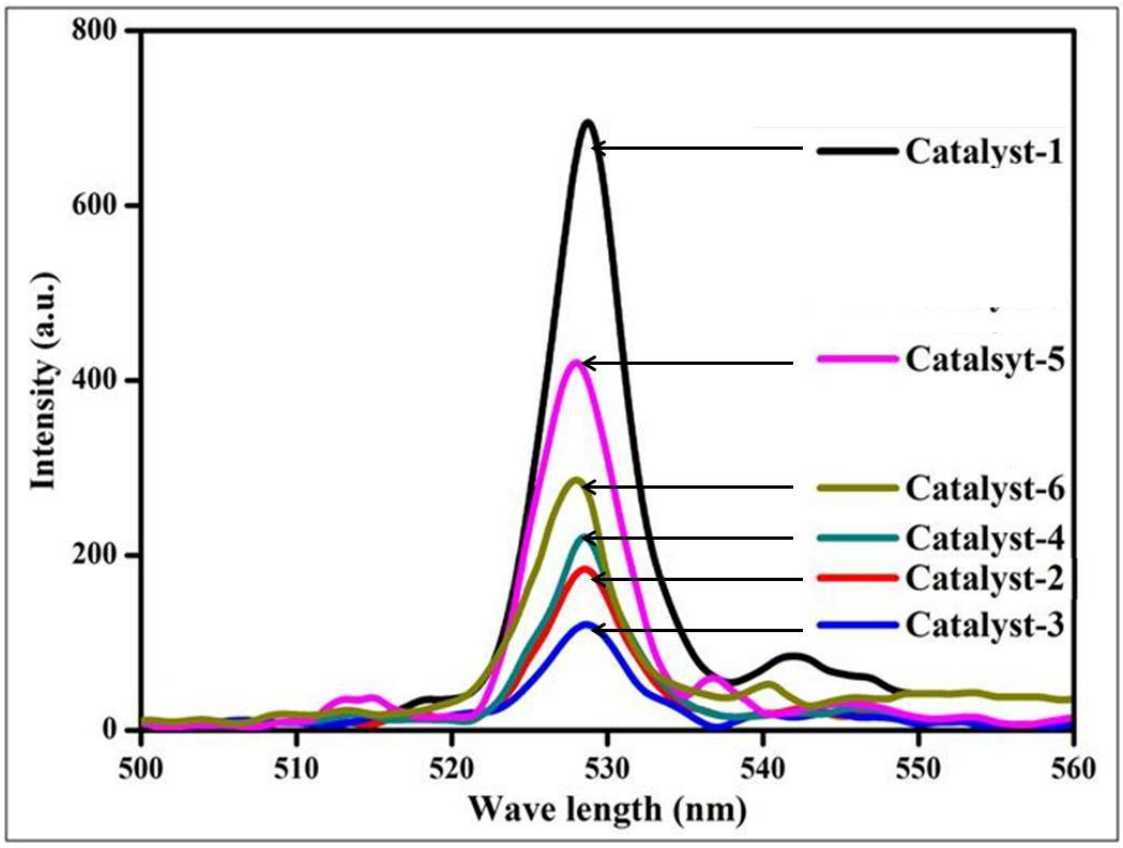


**Figure 4.7:** Photoluminescence spectra of various catalysts.

When, CdS is excited by light photons ($E_{photons} > E_{bandgap}$) or by electron beam, principal emissions are observed at ~520 nm i.e. a rather narrow, edge luminescence often known as green luminescence [313]. Kroger et al. [314] suggested that the green emission resulted from the recombination of free holes and free electrons through excitonic states. Vuylsteke et al. [315] also remarked that the green emission at 524 nm (2.38 eV) occurs through direct recombination of CB electrons and VB holes. Therefore, the PL intensity has been reported to correlate with the electron-hole recombination [316]. If the photogenerated electron and holes are prevented to recombine, the intensity of photoluminescence will be less. It also means that electrons and holes shall be available for the chemical reaction. A comparison of the PL spectra of various catalysts show that the introduction of GO or rGO drastically decreased the

PL intensities of GO/rGO supported catalysts (catalyst–2 to 4) in comparison to unsupported CdS (catalyst–1). Even catalyst–5 and 6 had lower intensity compared to unsupported CdS. In fact, many photoelectrochemical measurements have confirmed that GO/rGO serves as electron acceptor and thus can improve electron transfer properties. For example, Lv et al. [198] demonstrated by using time-resolved emission spectra and photocurrent generated response measurement techniques that rGO embedded to semiconductor can efficiently accept electrons from the excited semiconductor and suppress the charge recombination. Li et al. [317] studied the photocurrent generation capability and the incident photon to current conversion efficiency of graphene-CdS, the improvement of efficiency was ascribed to electronic property of graphene and morphology. Cao et al. [192] have reported using time-resolved fluorescence spectroscopy that the graphene-CdS had a lower time constants due to the electron transfer from the excited CdS to the graphene. Wang et al. [318] also showed by using transient photo-voltage technique that graphene has a high ability to accept electrons. Therefore, it can be concluded that coupling GO/rGO with CdS can increase the electron acceptance and transport rate in the composite and therefore suppress the charge recombination.

Hence, greater the recombination more intense shall be the PL intensity. In other words, if PL intensity is less, more electrons should be available to carry out the reduction of water to $H_2$. The above observation can be explained on the basis of high conductivity and the relative position of Fermi level of GO and rGO. The lowest conduction band potential of CdS and the Fermi level of rGO are –0.65 V and –0.08 V versus NHE, respectively [191,319]. Therefore the photogenerated electrons of CdS could be effectively transferred to GO or rGO.

It is also observed that catalyst–2, 3, 4 and catalyst–5 & 6 all had same composition still the PL intensities were different. The lowest PL intensity observed in catalyst–3 implies that recombination of electron-hole pairs were minimum. For transfer of electron from CdS to GO/rGO an intimate contact at the interface would be necessary. As stated earlier (Section 4.2), electronic interaction between the n-orbital of the sulphur of CdS and $\pi^*$ orbital of GO/rGO may take place, which would results into formation of a heterojunction at the interface. FTIR studies have indicating that an interfacial chemical interaction exists between carbon of GO/rGO in catalyst–2 & 3 and sulphur of CdS. Such an interaction was largely nonexistent in case of catalyst–4 prepared by hydrothermal technique.

### 4.6 Diffuse reflectance studies

The diffuse reflectance spectra of all the catalysts are recorded for the range of 450 to 700 nm and are shown in the Fig. 4.8. It is observed that for catalyst–1 there is a sharp increase in the absorbance starting at ~540 nm. Such a sharp increase in absorbance indicates onset of band gap excitation. However, such a sharp rise is not observed in catalysts–2, 3 and 4. These catalysts were CdS supported on GO or rGO. It is also observed that GO and rGO supported catalysts have a rather continuous absorption in the range of visible light. This effect is more pronounced in catalyst–3.In earlier research works, an extended optical absorption has been also observed in graphene based photocatalyst. Peng et al. [199] ascribed the enhanced visible light response due to increment in surface electric charge of CdS in photocatalyst due to presence of GO/rGO. Gao et al. [320] also attributed that graphene-CdS had a continuous absorbance in the visible range compared with bare CdS which was because

graphene could enhance the surface electrical charge of CdS. Wang et al. [321] also reported that enhancement of absorption in visible-light due to increment of surface electrical charge of host catalyst in presence of doped carbon material (MWNT). Xu et al. [322] reported that ZnO/graphene composite showed higher absorbance in visible light region due to an increase of surface electric charge of the oxides in the composite due to graphene introduction. We also think that a greater photo response observed in catalyst–3 is due to surface electric charge on the CdS due to the presence of GO/rGO.

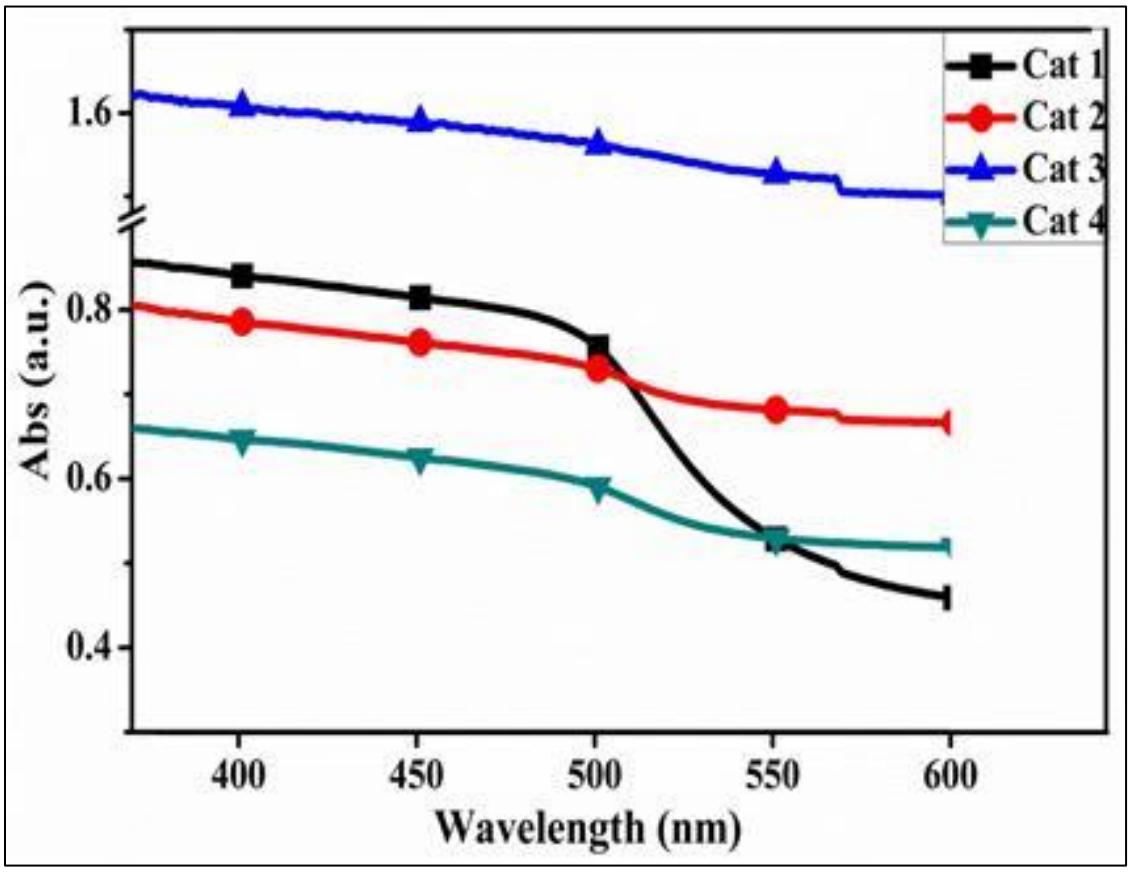


**Figure 4.8:** Diffuse reflectance spectra of catalysts.

The direct band gap was also calculated by plotting $(\alpha h\nu)^2$ vs. $h\nu$, where $\alpha$ is the absorbance [Fig. 4.9]. The intercept on the $x$-axis yielded the value of band gap.

However, it was difficult to estimate the bandgap accurately owing to the continuous increase in absorbance in GO & rGO supported catalysts [catalyst–2, 3 and 4]. The calculated values of band gaps are 2.48, 2.32 2.18 and 2.22 eV for the catalyst 1-4, respectively [Table 4.6].

**Table 4.6:** Band gap of CdS in various catalysts.

| Catalyst | Band gap (eV) |
|---|---|
| Catalyst–1 | 2.48 |
| Catalyst–2 | 2.32 |
| Catalyst–3 | 2.18 |
| Catalyst–4 | 2.22 |

It is seen that incorporation of GO or rGO has resulted into narrowing of bandgap. Narrowing of bandgap has been also observed by many earlier workers. Zhang et al. [323] attributed this phenomenon due to chemical bonding between host catalyst and carbon. Chai et al. [324] also observed narrowing band gap with enhanced visible light absorption. They ascribed it to interfacial interaction between CdS and carbon species. Pan et al. [212] reported that graphene doped CdS showed higher photocatalytic activity. They reported that absorption edge is red shifted and band gap is also narrowed due to substitutional doping of carbon within CdS. Wu et al. [325] reported shifting in absorption edge in rGO doped CdS. They explained that this was due to stronger coupling between rGO & CdS and better distribution of CdS on rGO. Li et al. [201] also reported augmented visible light response after the introduction of graphene into CdS leading enhanced photocatalytic activity. Zhang et

al. [326] also ascribed this to electronic interaction of composite with GO. Conclusively, all these have attributed such narrowing of bandgap to the interfacial interaction of CdS with GO/rGO. Lee et al. [327] have reported that chemical bonding between semiconductor and GO/rGO can introduce a localized state within the bandgap of the semiconductor causing bandgap narrowing or analogously, a red shift in the absorption edge. We also concluded that the chemical interaction between CdS and rGO has created a localized state with narrowing of band gap as shown in Fig. 4.10.

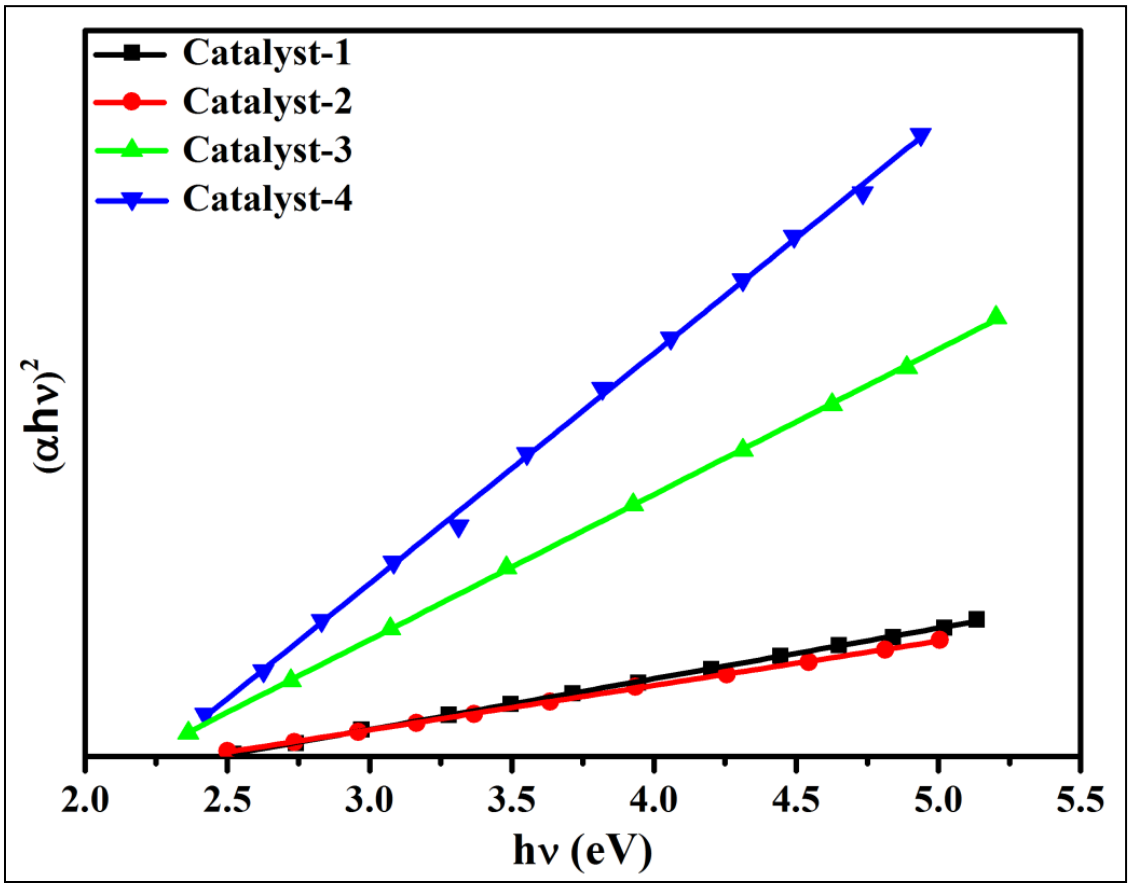


**Figure 4.9:** Bandgap of CdS in catalysts.

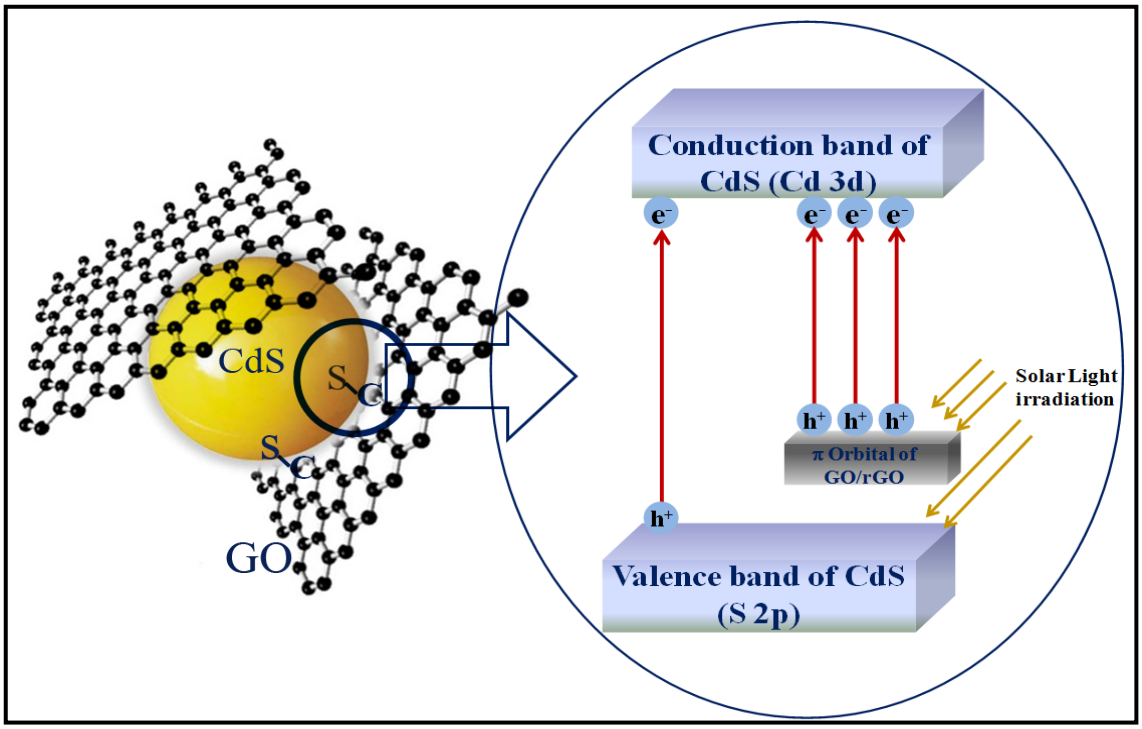


**Figure 4.10:** Schematic illustration for rGO-CdS photocatalysts (the magnified illustration is the transfer charge carriers between CdS and GO/rGO).

It is observed that both the phenomenon i.e., the narrowing the bandgap and enhanced absorption were more pronounced in catalyst–3. It should also be mentioned that catalyst–4 prepared by hydrothermal technique, a method mostly reported in the literature by many workers showed inferior absorption as well as negligible narrowing of band gap compared to the catalyst–3. It is in order to mention that photoluminescence studies also indicated significantly lower recombination of photogenerated electron-hole pairs in catalyst–3. Therefore, it may be concluded that a higher absorption and a greater interfacial interaction between CdS and rGO observed in catalyst–3 prevented the charge recombination and made a larger number of electrons available for the reaction.

## 4.7 XPS Studies

X-ray photoelectron spectroscopy (XPS) was carried out for surface characterization of samples. The C1s peaks are shown in Fig. 4.11. The peaks were de-convoluted using Lorenutzian Gaussian fitting [328]. It is clearly seen that carbon atoms are associated with different oxygen functional groups. The 284.6 eV peak is assigned for the carbon in the non-oxygenated ring, C=C bonds; at 286.4 eV peak is due to hydroxyl and epoxy, the 287.5 eV peak is due to C=O bond related to carbonyl and 288.7 eV for O=C–OH bond related to carboxyl [329,330]. Xu at al. [331] have reported that the peak at 285.6 eV can also be due to C–S bond. However, due to overlapping peaks the C–S peak could not be uniquely identified from the C1s peak. The relative intensity of C=C peak (284.6 eV) with respect to all other carbon peaks taken together was calculated and shown in Table 4.7.

**Table 4.7:** Peaks intensity ratio of C=C XPS peak for all catalysts.

| **Sample** | **Relative intensity of C=C* peak** |
|---|---|
| GO | 1.19 |
| rGO | 2.43 |
| Catalyst–2 | 1.79 |
| Catalyst–3 | 3.13 |
| Catalyst–4 | 2.76 |

*Ratio of peak height of C=C peaks to ∑peak heights of all oxygenated carbon 1s peaks.

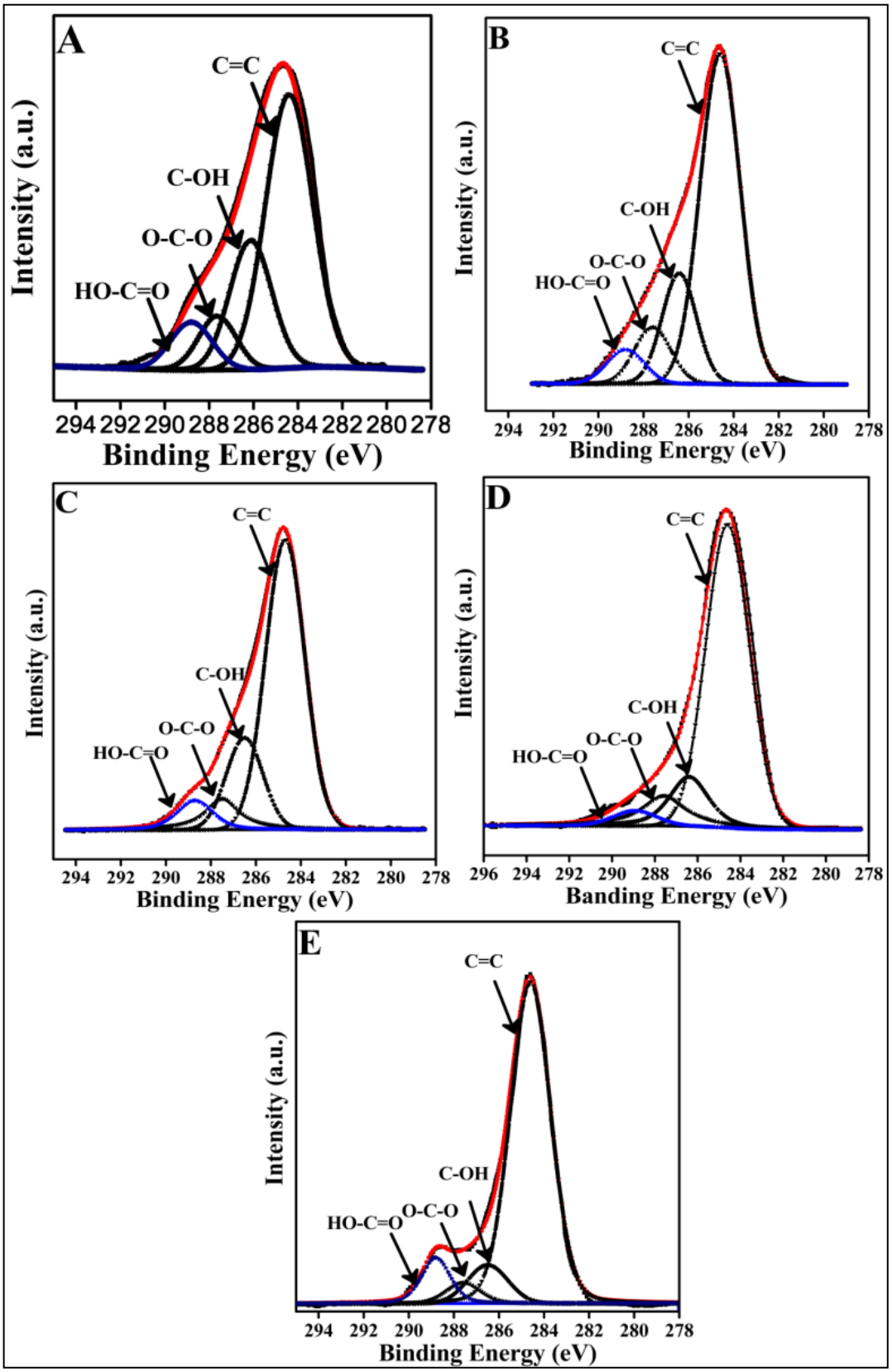


**Figure 4.11:** The C 1s XPS spectra of GO (A), rGO (B), catalyst–2 (C), catalyst–3 (D), catalyst–4 (E) including the multiple sub-peaks decomposed by Lorenutzian Gaussian fitting.

It is simply the ratio of peak height of C=C peak to the summation of all peak heights. It is seen that the ratio is more in rGO compared to GO indicating that the process adopted for reduction of GO to rGO had been successful. It is further observed that incorporation of CdS on GO/rGO has further improved this ratio (compare catalyst–2 with GO and catalysts–3 & 4 with rGO). It means that during the process of catalyst preparation, a few more oxygen containing functional groups have been removed.

The FTIR studies as reported earlier, have also led to the same observation. It is further seen from the Table 4.7 that the relative intensity of C=C peak is the highest for catalyst–3 which was CdS supported on rGO and prepared by the gas-solid reaction. The literature reports that higher the intensity of C=C peak more will be the electronic conductivity [332,333]. A higher electronic conductivity is also a requirement for a better charge separation and subsequently superior photocatalytic activity. In addition, it is also observed that catalyst–4, the C 1s peak intensity for O=C–OH bond [Fig. 4.11E] related to carboxyl has much higher intensity. It may be due to hydrothermal treatment during preparation of photocatalyst–4.

Fig. 4.12A shows the peaks of Cd 3d, where the detected major peaks for catalyst–1 which was unsupported CdS, at 405.3 and 412.0 eV is because of the $Cd_{3d5/2}$ and $Cd_{3d3/2}$ signal. Reported values in the literature [334-336] for $Cd^{2+}$ in CdS are also 405.1 & 412.1 eV for $Cd_{d5/2}$ and $Cd_{d3/2}$ respectively.

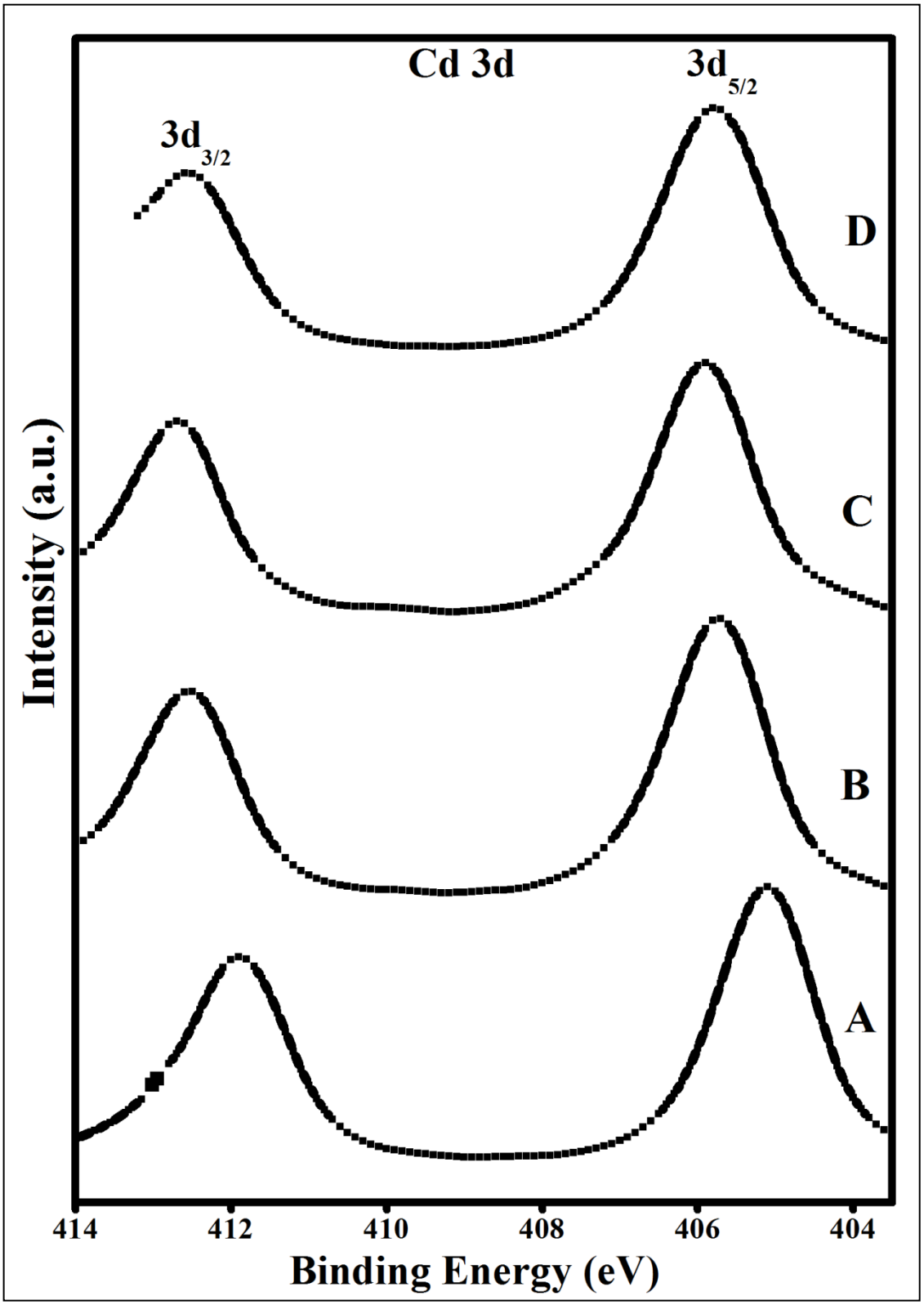


**Figure 4.12:** The Cd 3d XPS spectra of catalyst–1 (A), catalyst–2 (B), catalyst–3 (C), catalyst–4 (D).

Positive shifts in peak positions have been observed in case of catalysts–2, 3 and 4 (Fig. 4.12B, Fig. 4.12C and Fig. 4.12D). These catalysts were CdS supported on GO/rGO. The shift in peak position confirms chemical interaction between CdS and support GO/rGO as indicated before by the FTIR analysis. Further, these shifts are 0.38, 0.6 and 0.4 eV for catalysts–2, 3 and 4 respectively. It is in order to mention that catalysts–2 and 3 were prepared by the gas–solid reaction whereas catalyst–4 was prepared by the hydrothermal method. In addition, for the catalyst-2, support was GO whereas for the catalysts–3 & 4, the support was rGO. From the analysis of the shifts in binding energies it is observed that the support and the preparation technique both cause shift in binding energies and hence, influence the chemical interaction at the interface. The use of rGO and a preparation method involving the gas–solid reaction had resulted in the highest shift in the binding energy (catalyst–3). It is further observed that as reported above the activities of catalysts were in the order catalyst–3> catalyst–4> catalyst–2. The shift in binding energy also follows the same order, i.e., catalyst–3> catalyst–4> catalyst–2. Thus, it is concluded that the activity of catalysts correlated with the shift in binding energy or the extent of chemical interaction at the interface.

Nature of interaction in these catalysts was investigated by etching sample in–situ by argon ion bombardment on the surface for various time intervals and depth profiling was obtained. These results are shown in Fig. 4.13, 4.14 and 4.15 for catalysts–2, 3 and 4, respectively. In all the catalysts it is observed that the BE's shift to lower value and become closer to the BE of $Cd^{2+}$ in unsupported CdS with increase in etching time. The difference in BE with respect to unsupported CdS are shown in Fig. 4.16. It is evident that as the surface layers are progressively removed, the interaction of CdS with the support diminishes. Therefore, the chemical interaction between CdS and the support

GO/rGO is existent near the interface only and the greatest interaction has taken place in catalyst–3.

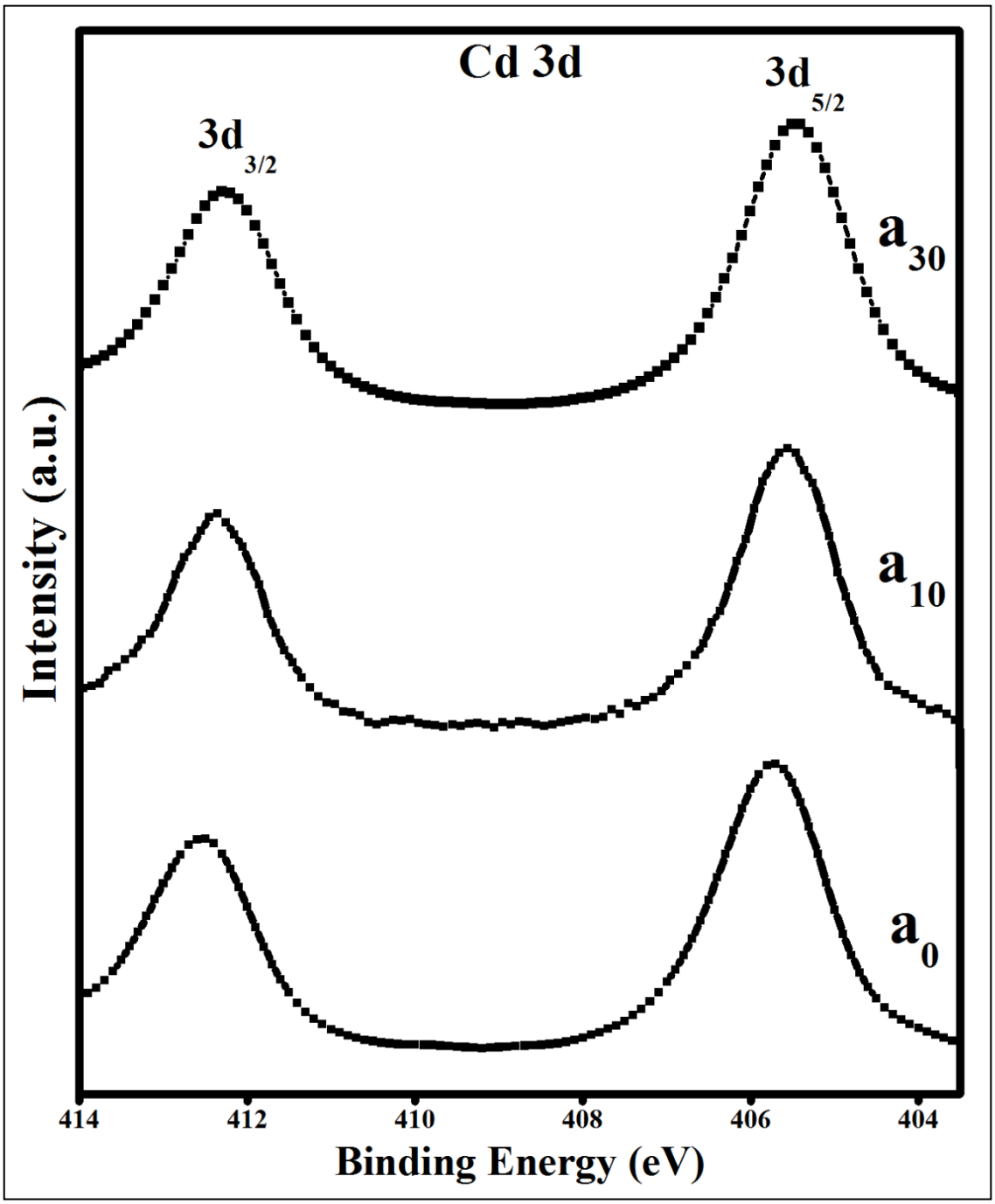


**Figure 4.13:** Depth Profile for catalyst–2, Cd 3d after etching at various time intervals, ($a_0$- without etching, $a_{10}$- etched for 10 s, $a_{30}$- etched for 30 s).

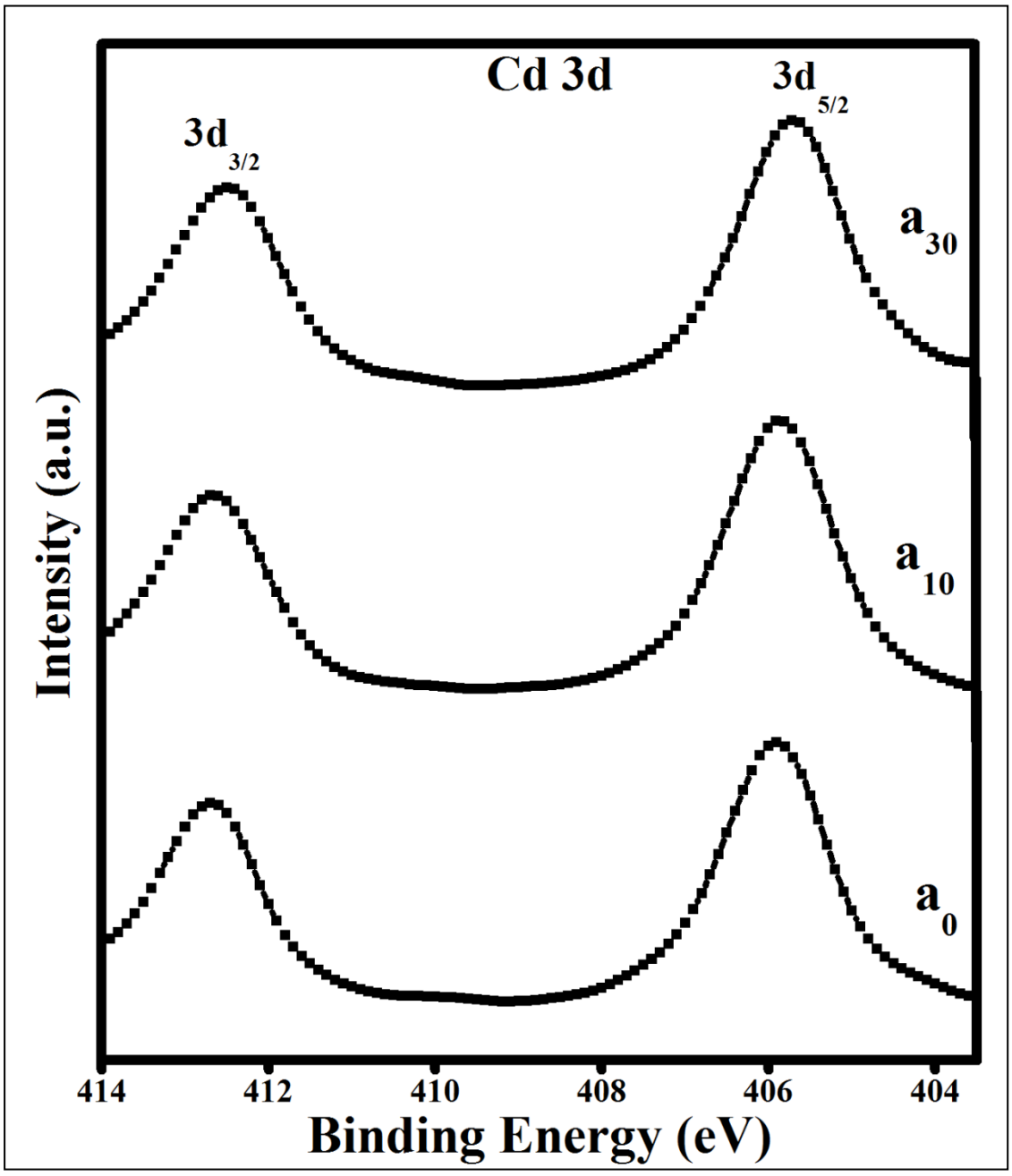


**Figure 4.14:** Depth profile for catalyst–3, Cd 3d after etching at various time intervals, ($a_0$- without etching, $a_{10}$- etched for 10 s, $a_{30}$- etched for 30 s).

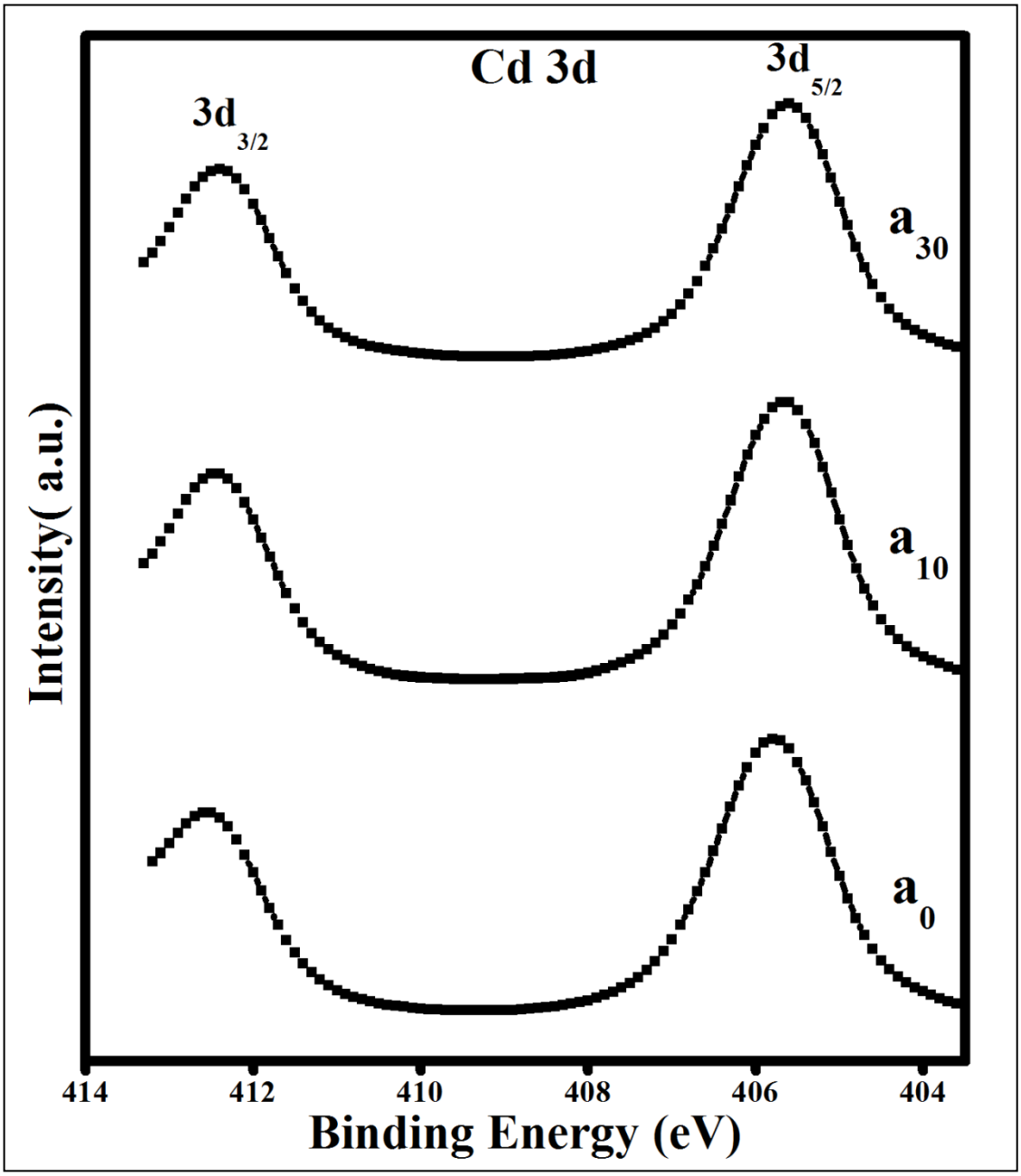


**Figure 4.15:** Depth profile for catalyst–4, Cd 3d after etching at various time intervals, ($a_0$- without etching, $a_{10}$- etched for 10 s, $a_{30}$- etched for 30 s).

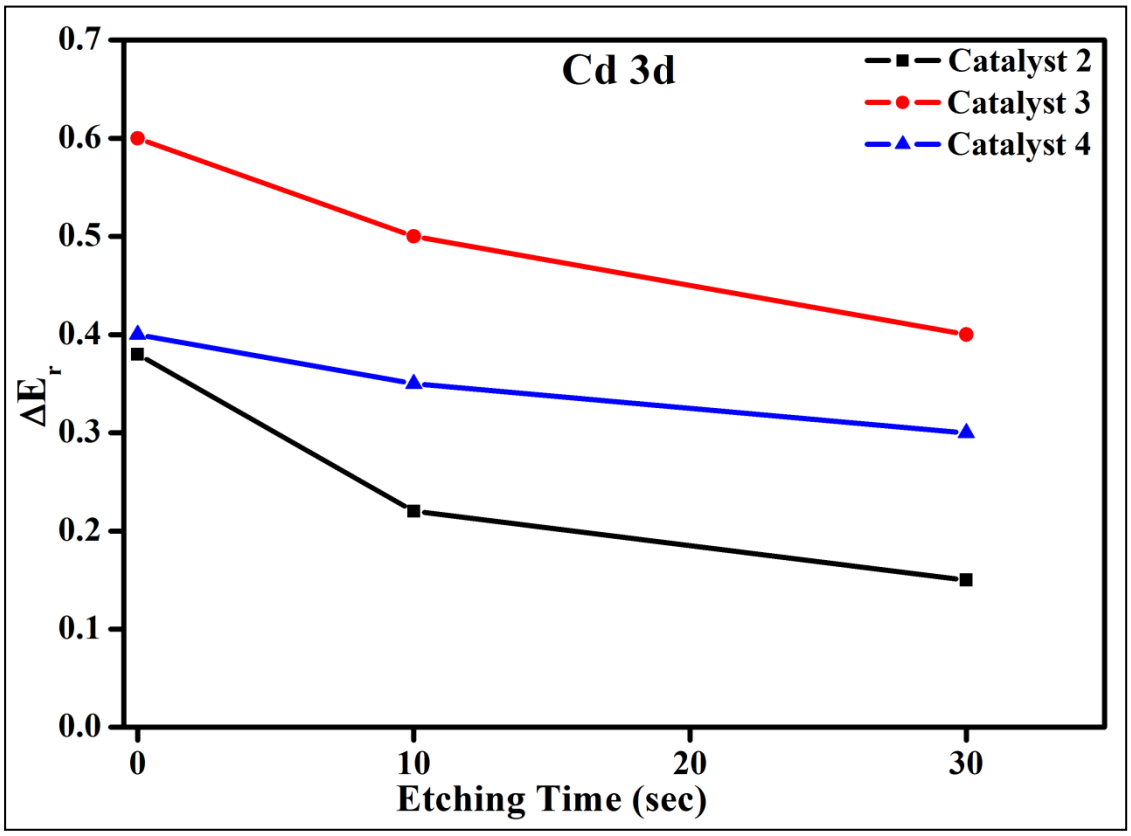


**Figure 4.16:** ΔE vs. etching time for Cd 3d, ΔE = Difference between binding energy of respective catalyst for Cd $3d_{5/2}$ and binding energy of catalyst–1 for Cd $3d_{5/2}$ after etching at various time interval.

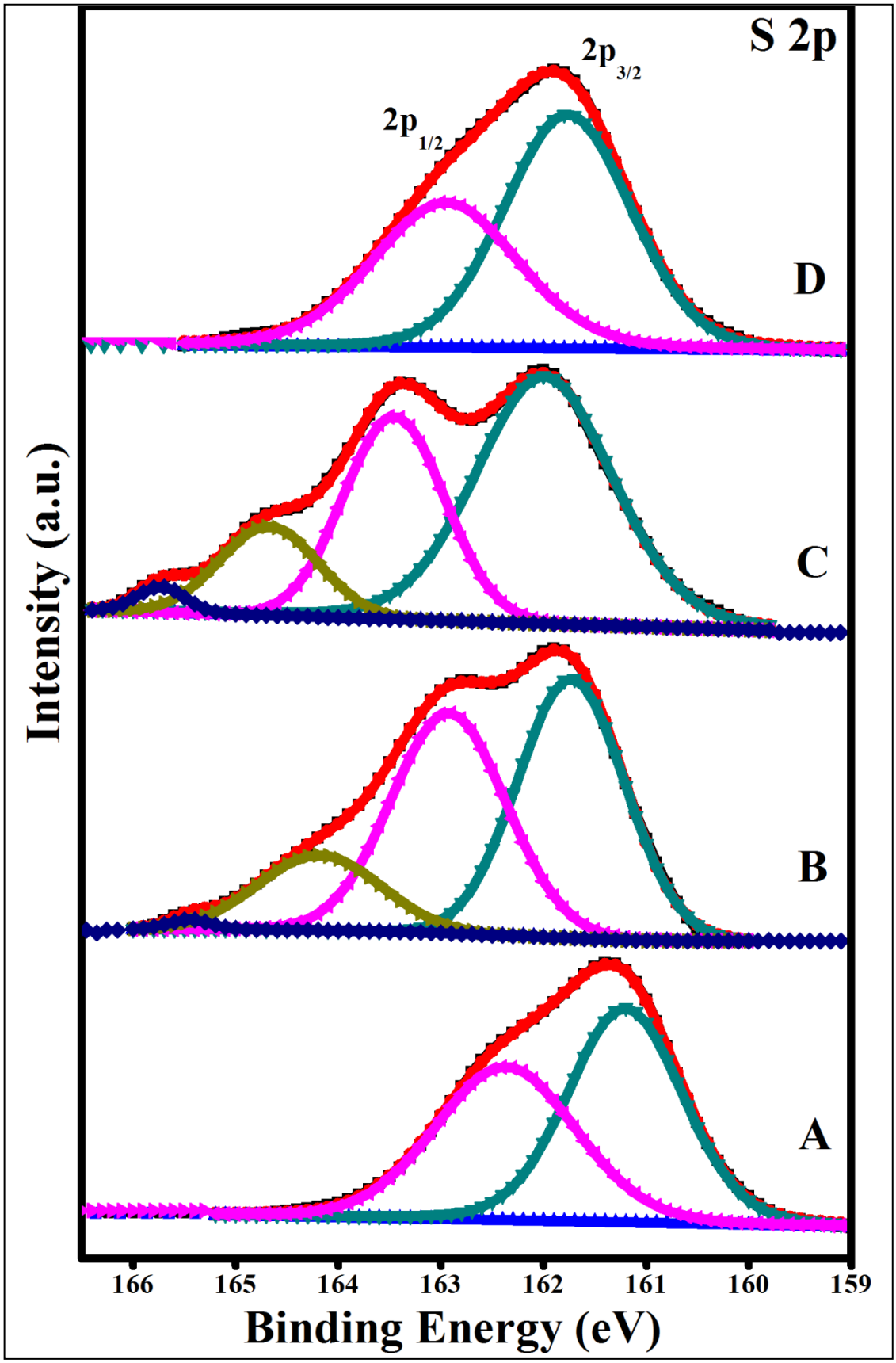


**Figure 4.17:** The S 2p XPS spectra of various catalysts (A): catalyst–1, (B): catalyst–2, (C): catalyst–3, (D): catalyst–4.

The S 2p spectra of CdS of catalysts–1 to 4 are shown in Fig. 4.17. The peaks were carefully deconvoluted and are also shown in the figure. Both the original and deconvoluted peaks are shown. Catalyst–1 (unsupported CdS) and catalyst–4 (prepared by hydrothermal technique) had a single doublet. Whereas catalyst-2 and 3 which were GO and rGO supported CdS and prepared by impregnation followed by gas-solid reaction had two well resolved doublets. The peak positions (binding energy) have been reported in Table 4.8. For catalyst–1, there are two peaks at 161.2 and 162.4 eV which correspond to $2p_{3/2}$ and $2p_{1/2}$ peaks of $S^{2-}$ of CdS. These values match with the reported values of $S^{2-}$of CdS i.e. 161.3 and 162.5 [337,338]. In the case of catalysts–2, 3 and 4, the peaks position of first doublet are at 161.7 & 162.95 eV for catalyt–2, 162.3 & 163.6 eV for catalyst-3 and 161.7 & 163.1 for catalyst-4. These values are close to $2p_{3/2}$ and $2p_{1/2}$ peaks of $S^{2-}$ of CdS as reported in the literature. Therefore these peaks have also been assigned to $S^{2-}$of CdS. However, the BE of $2p_{3/2}$ peaks of the first doublet in catalyst–2, 3 & 4 show significant variation. The BEs become more positive for GO/rGO supported CdS. Such a shift in BE is conclusive evidence of interfacial chemical interaction between CdS and GO/rGO through $\pi^*$ orbital of GO/rGO and *n* orbital of S or CdS. Due to this chemical interaction, as explained below, the net charge on sulphur ion become less as compared to that of sulphur ion in unsupported CdS and therefore a positive shift in BE are observed. Further observation shows that such a shift has taken place to a greater extent in catalyst–3 which also showed the highest activity. This is in line with the accepted mechanism that a greater chemical interaction at the interface would promote an efficient separation of charges.

It is also to be mentioned that CdS prepared by impregnation followed by high temperature reaction has *n*-type semiconductivity whereas GO/rGO has p-type semiconductivity, therefore, chemical interaction at the interface as reported above may result into formation of *p*-*n* heterojunction in catalyst–2 and 3. Further, catalyst–3 had a higher activity compared to catalyst–2 because catalyst–3 was rGO supported which has an additional attribute of high electron mobility. The high electronic conductivity has been shown experimentally by Impedance spectroscopy and presented below. Therefore, high activity of catalyst–3 is as a result of high electron conductivity of support rGO and chemical interaction at the interface.

**Table 4.8:** Results of XPS analysis of sulphur peaks.

| **Catalyst** | **Position of sulphur (2p) peaks (eV)** | | | |
|---|---|---|---|---|
| | **First doublet** | | **Second doublet** | |
| | **$p_{3/2}$** | **$p_{1/2}$** | **$p_{3/2}$** | **$p_{1/2}$** |
| 1 | 161.2 | 162.4 | - | - |
| 2 | 161.7 | 162.95 | 164.4 | 165.5 |
| 3 | 162.3 | 163.6 | 164.7 | 165.7 |
| 4 | 161.7 | 163.1 | - | - |

It is further observed from Fig. 4.17 that, an additional doublet of sulphur has appeared for catalyst–2 and 3. This second doublet appears at 164.4 & 165.5 and ~164.7 & ~165.7 eV for catalyst–2 and catalyt–3, respectively. It is reported

in the literature that elemental sulphur has the binding energy at 164.3 eV [339]. The literature [340,341] also reports BE of 163.8 eV for C–S species and C–S–C type sulphur. Accordingly, on the basis of this discussion, these second doublet observed in catalyst–2 and 3 have been ascribed to formation of C–S type bond. This bond formation is due to sulphur doping [as discussed section 4.2]. It is in order to mention that FTIR studies had also indicated presence of carbon-sulphur bond in these two samples.

Further analysis of $S^{2-}$ peaks of CdS in catalysts reveals that the peak positions in catalysts–2, 3 and 4 have shifted to higher values in comparison to unsupported CdS (catalyst–1). As discussed above, the change in binding energy is due to a chemical interaction between CdS and the support rGO/GO. Shift in the binding energies and consequently the interaction in seen to be highest in catalyst–3 where rGO was used as a support and the catalyst was prepared by a gas–solid reaction. This catalyst also showed the highest activity.

The effect of surface etching on the change in BE of $S^{2-}$ was also measured and are shown in Fig. 4.18, 4.19, 4.20. It is seen that the positive shifts in binding energy diminish with the etching time [Fig. 4.21]. It clearly indicated, as concluded above also, that the interaction between CdS and GO/rGO was a surface phenomenon and did occur at the interface of the two, i.e., CdS and GO/rGO. The literature reports the possibilities of interaction between CdS and rGO/GO through $\pi^*$ orbital of C and *n* orbital of S of CdS. Peng at al. [199] reported that possible interaction between photocatalyst and carbon material such as $\pi \rightarrow \pi^*$ and $n \rightarrow \pi^*$ between the n orbital of the CdS and MWCNTs. Liu et al. [302] reported that the electronic transition of $\pi \rightarrow \pi^*$ of MWCNTs and $n \rightarrow \pi^*$ between the n-orbital of the sulphur species of photocatalyst. We also

propose such interaction in catalysts–2, 3 and 4. The extent of this interaction is more when rGO is used as a support and catalyst is prepared by the gas–solid reaction.

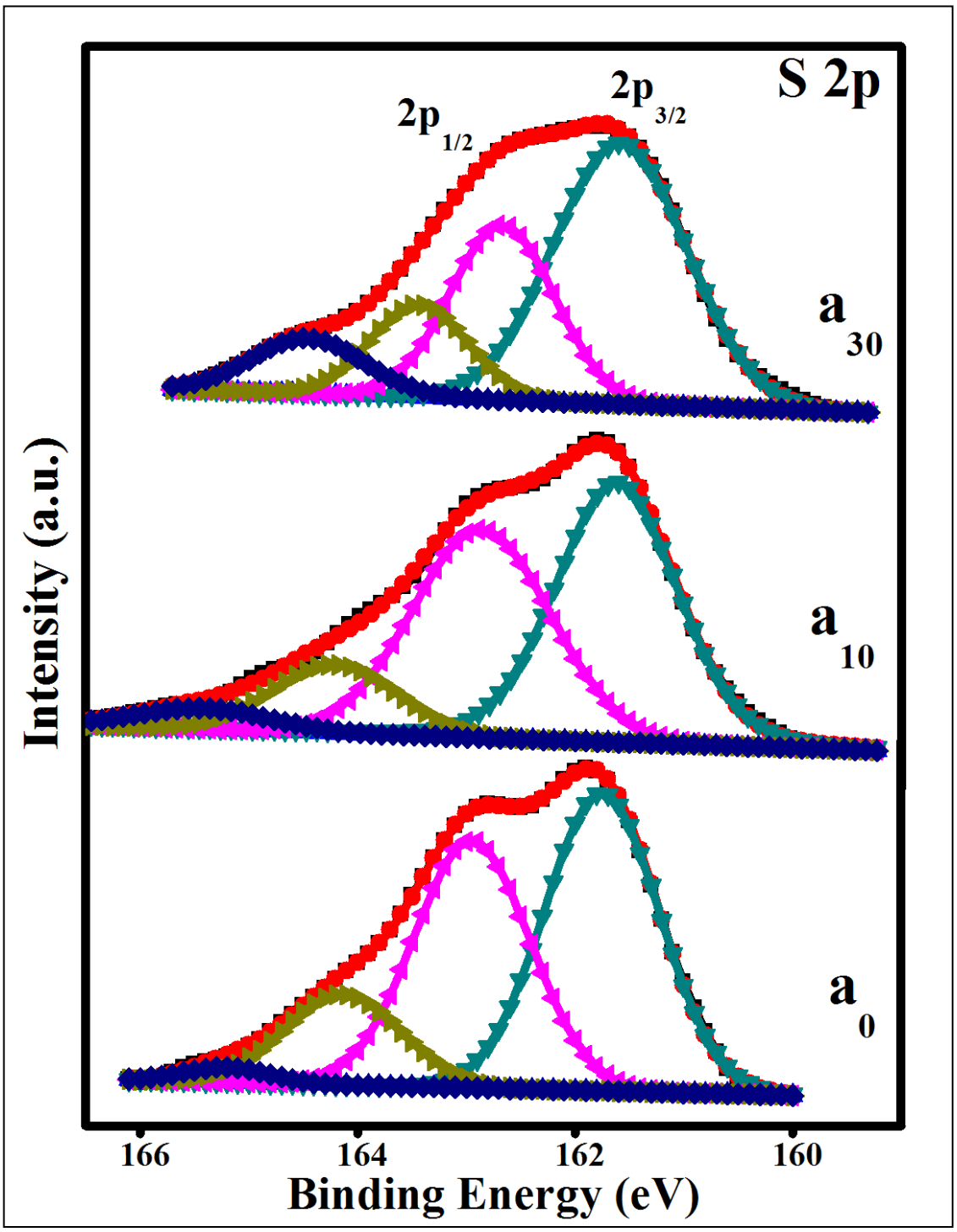


**Figure 4.18:** Depth profile for catalyst–2 S 2p after etching at various time intervals ($a_0$- without etching, $a_{10}$- etched for 10 s, $a_{30}$- etched for 30 s).

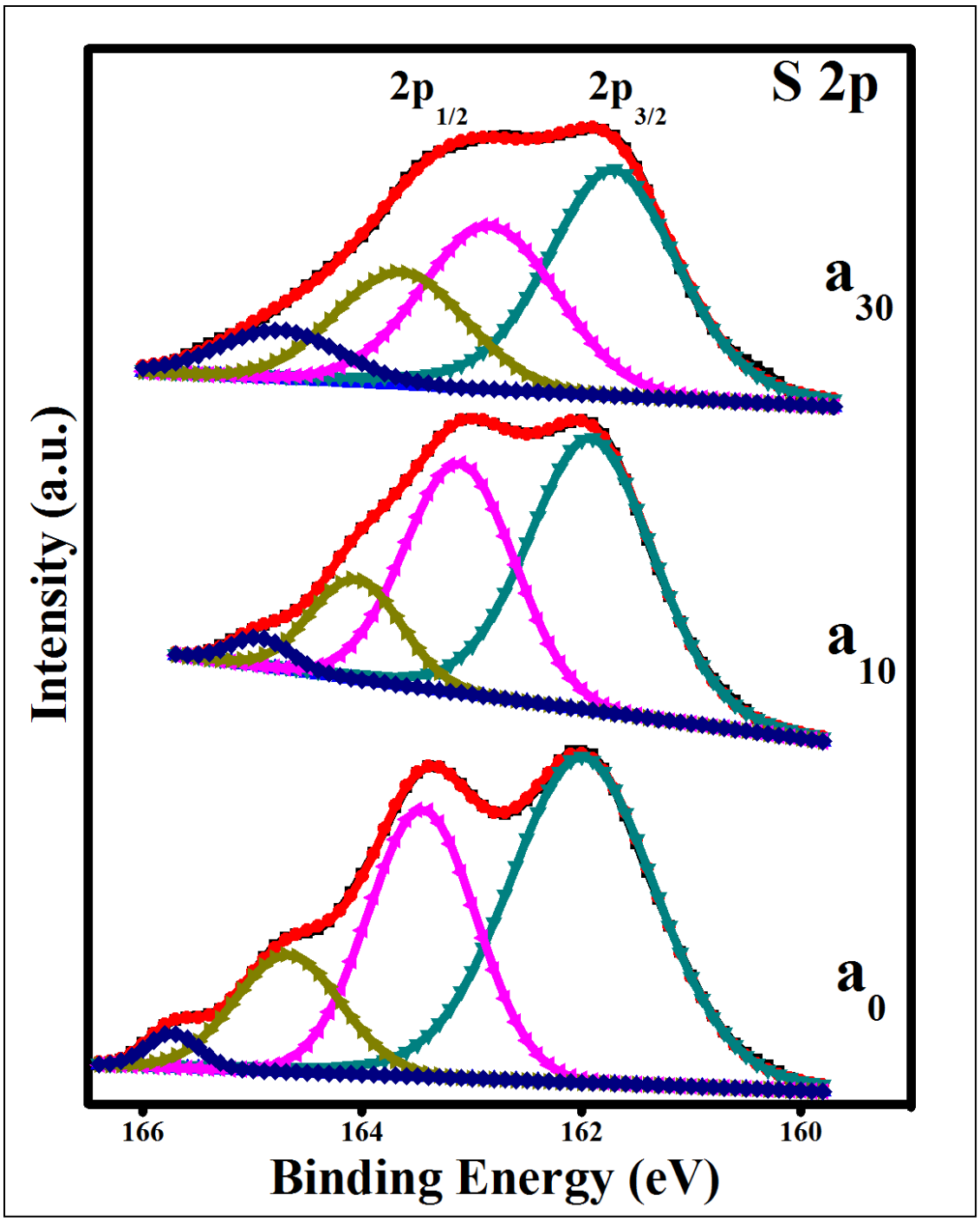


**Figure 4.19:** Depth profile for catalyst–3 S 2p after etching at various time intervals ($a_0$- without etching, $a_{10}$- etched for 10 s, $a_{30}$- etched for 30 s).

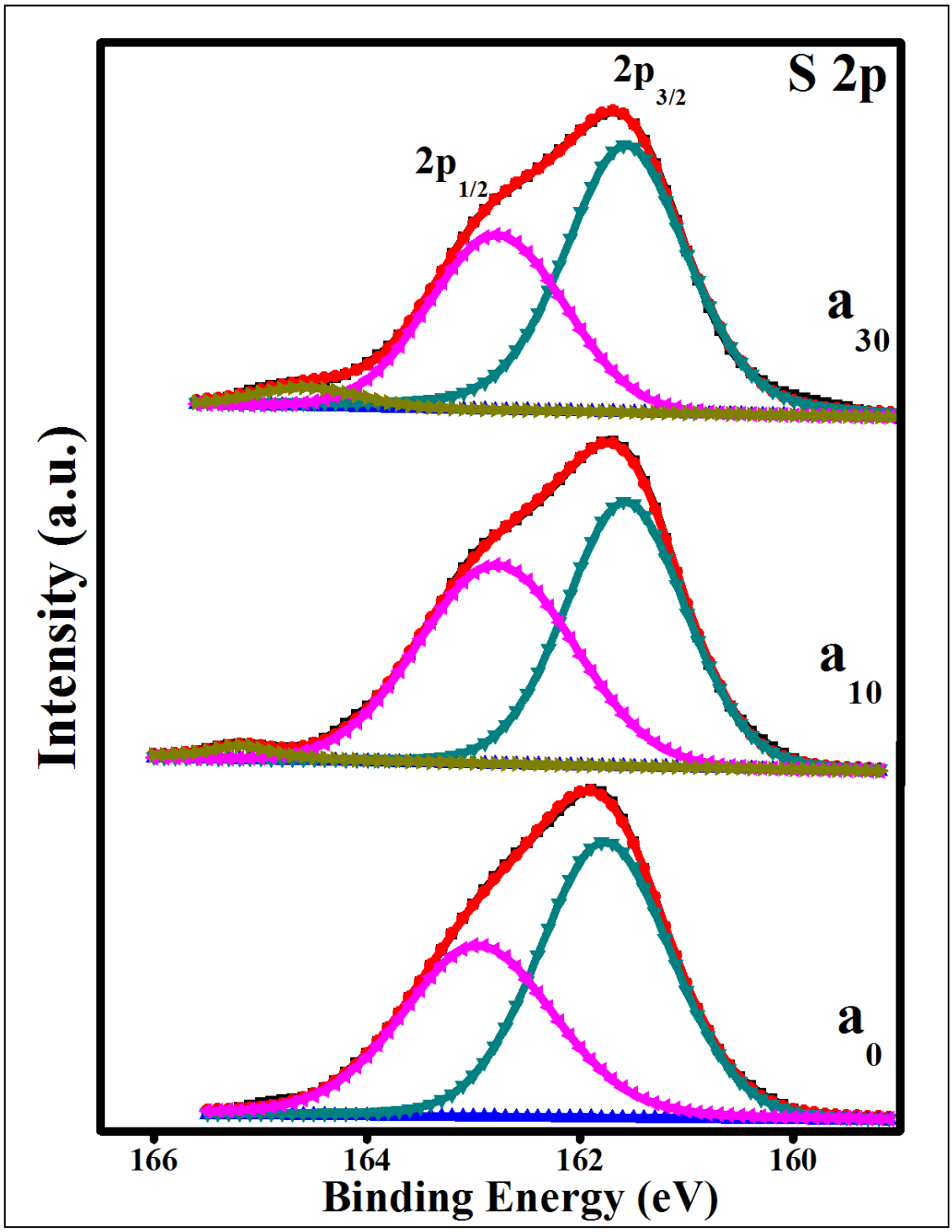


**Figure 4.20:** Depth profile for catalyst–4 S 2p after etching at various time intervals ($a_0$- without etching, $a_{10}$- etched for 10 s, $a_{30}$- etched for 30 s).

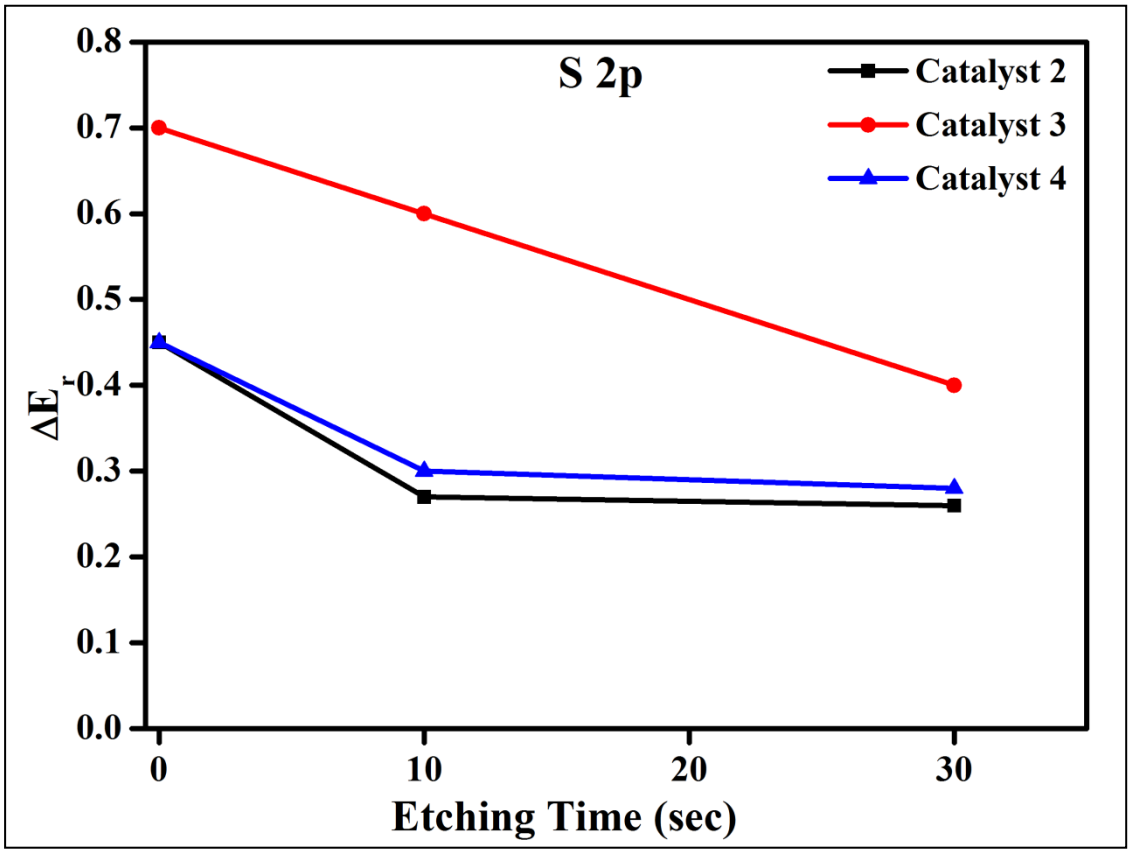


**Figure 4.21:** ΔE vs. etching time for S 2p, ΔE = Difference between binding energy of respective catalyst for S $3p_{3/2}$ and binding energy of catalyst–1 for $S2p_{1/2}$ after etching at various time interval.

The above results can be explained on the basis of following postulates. Presence of highly electronegative oxygen atoms on the surface of rGO/GO will cause polarization of charges on $Cd^{2+}$ and $S^{2-}$ as shown below:

$Cd^{2+\delta_1} - S^{-2+\delta_2} \cdots C^{-(\delta_1+\delta_2)}$, $\delta_1$, and $\delta_2$ are positive polarization charge.

Consequently, at the interface, sulphur will become less negatively charged and cadmium more positively charged. Hence, the binding energies of both $Cd^{2+}$ as well as $S^{2-}$ will have positive shifts in comparison to where no such interaction existed between CdS and GO/rGO. This chemical interaction facilitates transfer of electrons from CdS to rGO and therefore recombination of photogenerated electron-holes is restricted. In such

a condition more electrons shall become available for transfer to the liquid-solid interface and subsequent reactions for hydrogen production.

### 4.8 Temperature programmed oxidation studies

Although the temperature-programmed oxidation technique has been carried out to study metal support interaction as reported in the literature [342,343], we carried out TPO of CdS supported GO/rGO to understand their interaction. The results are shown in Fig. 4.22 & 4.23.

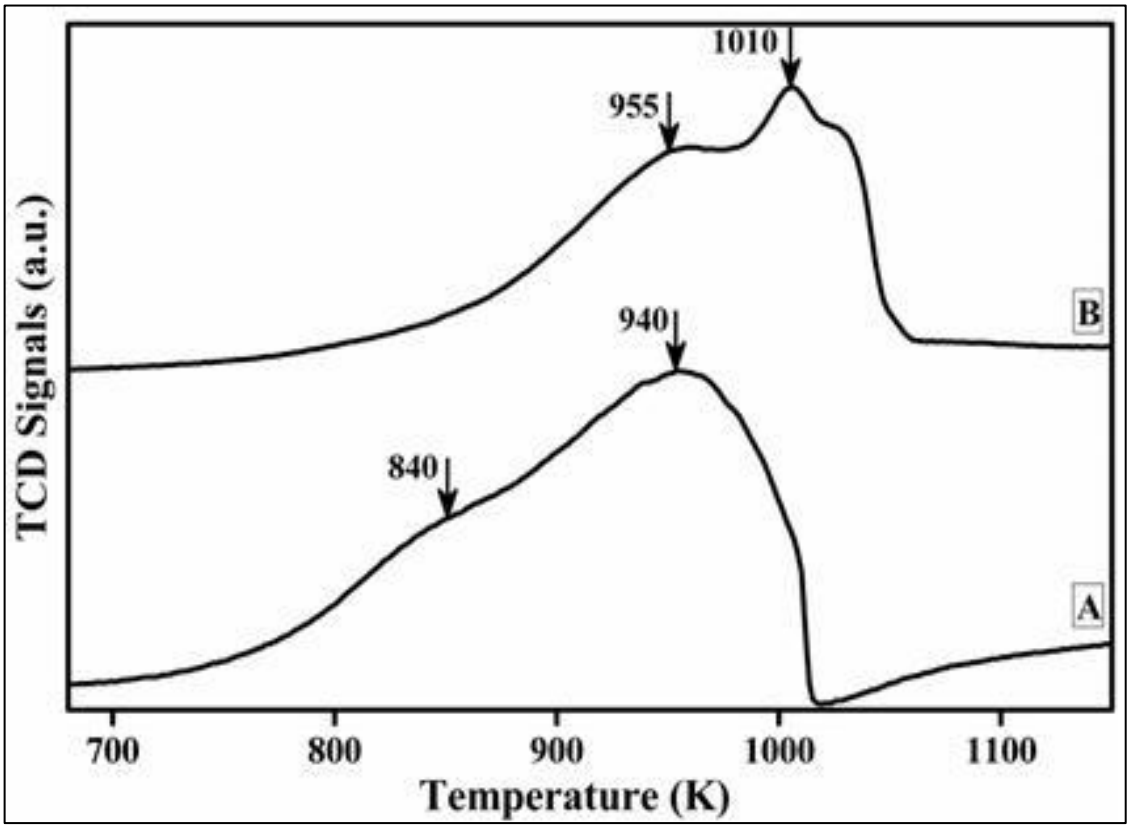


**Figure 4.22:** Temperature program oxidation peaks of samples, A: rGO, B: catalyst–1.

It is observed that for unsupported CdS, the peaks in the profile appear at 955 K and 1010 K and for rGO/GO peaks were observed at 840 K and 940 K

[Fig. 4.22]. The TPO profiles of catalyst–2, 3 and 4 had a total four peaks [Fig. 4.23]. On comparison with CdS the peaks appearing at temperature ~940 K and ~1000 K may be assigned to oxidation of CdS, whereas peaks appearing at ~840 K and ~930 K to the oxidation of GO/rGO. Though the TPO profiles are rather continuous and broad, still the shifts in peak position in catalyst–2, 3, and 4 may be observed, compared to CdS and GO/rGO. The shift in peak position is indicative of interaction between CdS and GO/rGO. The shift was greatest in catalyst–3 and least in catalyst-4, which was prepared by hydrothermal technique. These observations are in line with those of XPS as discussed above.

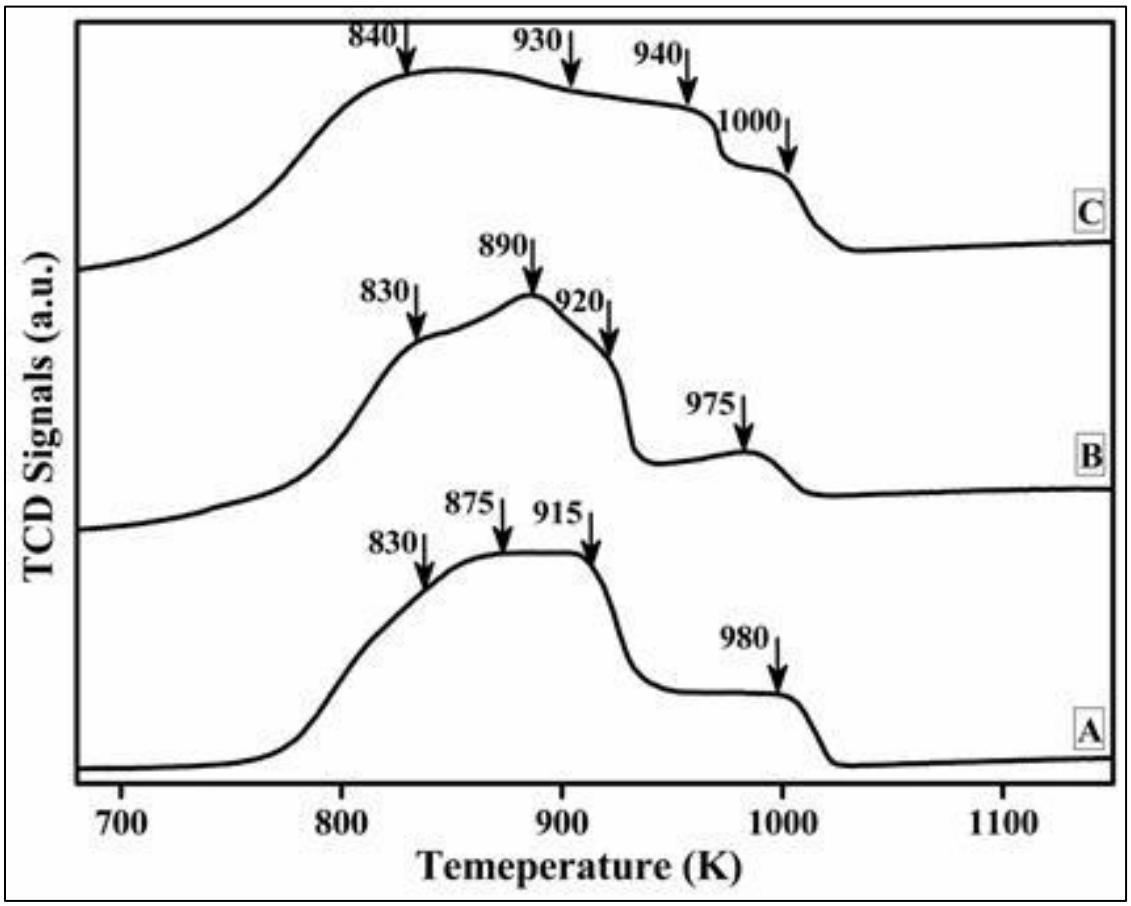


**Figure 4.23:** Temperature program oxidation peaks of catalysts, A: catalyst–2, B: catalyst–3, and C: catalyst–4.

## 4.9 EIS studies

Electrochemical impedance spectroscopy (EIS) of catalysts–2, 3 and 4 were carried out. The Nyquist analysis was performed to study charge carrier transport behaviour of catalysts. The results are shown in Fig. 4.24. The points on the left on the diagram correspond to high frequency. Frequency decreases as point progress from left to right in the diagram. It is known that low frequency intercept on the real axis corresponds to charge transfer resistance. Thus, a lower arc radius implies lower charge transfer resistance [344]. In other words it means a better electron transfer at solid–solid interface (CdS and support) and a faster transfer of electrons to the solid–liquid interface. It is seen that the arc radius is smallest for catalyst–3 followed by catalyst–4 and then catalyst–2. A better charge transfer will not only enhance the rate of reaction at solid-liquid interface but also result into a lower recombination of photogenerated electron hole pairs and both the factors shall contribute to the better photocatalytic activity.

We have reported that the photocatalytic activity of catalysts follow the trend, i.e., catalyst–3> catalyst–4> catalyst–2 which is in the reverse order of charge transfer resistant, i.e., catalyst–3< catalyst–4< catalyst–2. The charge transfer phenomena may be explained as given below:

Step I. Generation of electrons and holes in CdS:

$$\mathrm{CdS} \xrightarrow{h\upsilon} \mathrm{CdS}(e^-) + \mathrm{CdS}(h^+) \quad (4.4)$$

Step II. Recombination of electrons and holes:

$$\mathrm{CdS}(e^-) + \mathrm{CdS}(h^+) \rightarrow \mathrm{CdS} \quad (4.5)$$

Step III. Transfer of electron from CdS to support GO/rGO:

$$\mathrm{CdS}(e^-) \rightarrow \mathrm{GO/rGO}(e^-) \quad (4.6)$$

Step IV. Transfer of electron to solid-liquid interface:

$$GO/rGO(e^-) \rightarrow GO/rGO(e^-)_{surfcae} \quad (4.7)$$

Step V.

$$GO/rGO(e^-)_{surfcae} + \text{electrolyte} \rightarrow \text{hydrogen and other produts} \quad (4.8)$$

Steps II, III and IV will depend on the extent of chemical interaction and the charge transfer resistance. A high chemical interaction and small charge transfer resistance will enhance the rates of steps III and IV and suppress recombination (step II) and consequently rate of hydrogen production (step V) shall get enhanced.

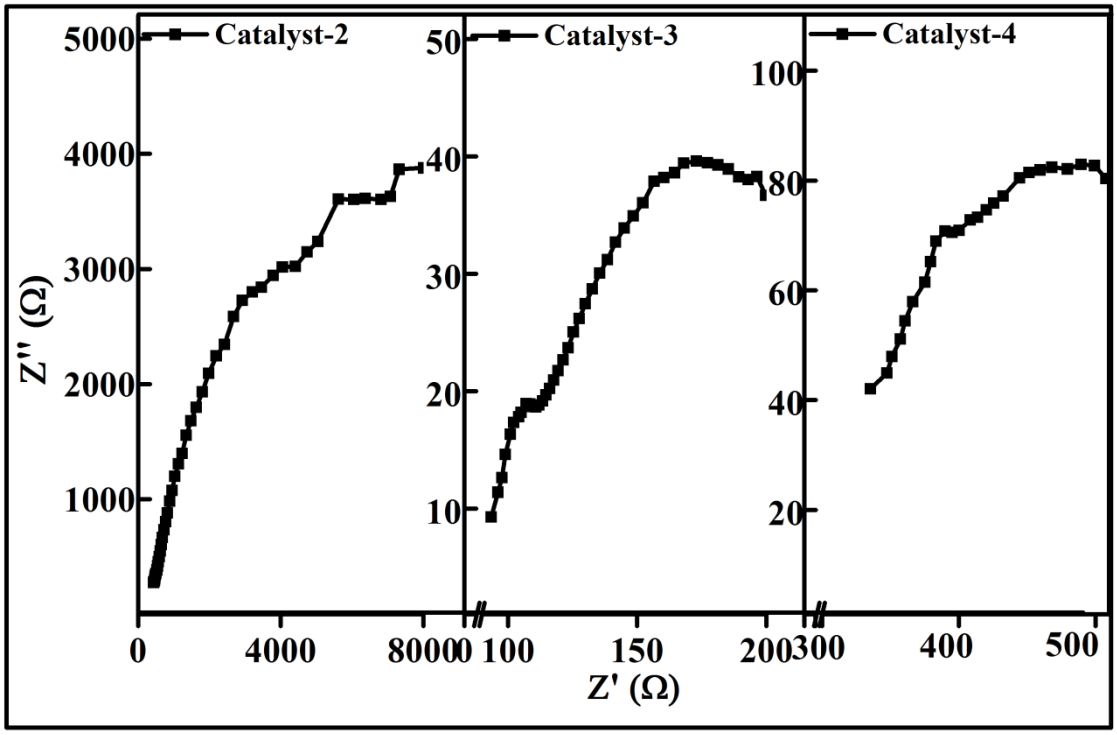


**Figure 4.24:** Nyquist plots recorded for various catalysts in electrolyte having sulphide and sulphite at room temperature.

Therefore, it may be concluded that the gas–solid reaction used for the preparation of CdS/rGO catalyst (catalyst–3) promoted formation of heterojunction by chemical

interaction between S of CdS and C of rGO at the interface of rGO and CdS. This heterojunction facilitated transfer of electrons from the conduction band of CdS to rGO. Subsequently rGO having higher electrical conductivity than GO resulted into faster transport of electrons to the solid-liquid interface. Because of the combined effect of these two phenomena, the CdS supported on rGO which was prepared by impregnation and followed by a gas–solid reaction showed superior activity.

## 4.10 Photocatalysis with ultrasound

In this subsection, results have been presented on the basis of experiments performed using ultrasound with photocatalysis for hydrogen production form water dissociation.

### 4.10.1Effect of ultrasonication

Experiments were carried out to study the effect of ultrasound on photocatalytic hydrogen production by water dissociation. The experimental details remained the same as given earlier for photocatalysis without ultrasound [section 4.3]. The only difference was that the magnetic stirrer was not used to keep particles suspended and an ultrasonic horn was introduced with its tip immersed in liquid and it produced ultrasound waves of frequency 20 kHz. The input power of ultrasound was 35 W. The ultrasonic wave was found to be sufficient to keep the particles suspended in the liquid.

Initially, experiments were carried out in dark and no hydrogen production was observed. It was reported in literature [345-347] that when ultrasound was applied in reaction, sonolysis of water alone could give reactive species (·H and ·OH) [discussed in sec 4.10.2]. These further produced $H_2$ and $O_2$, respectively. Since further, in our experiments, no oxygen was detected in the product gas. Therefore, the possibility of

dissociation of water by ultrasound was ruled out. Thus, the evolved hydrogen gas was by photocatalytic dissociation of water only.

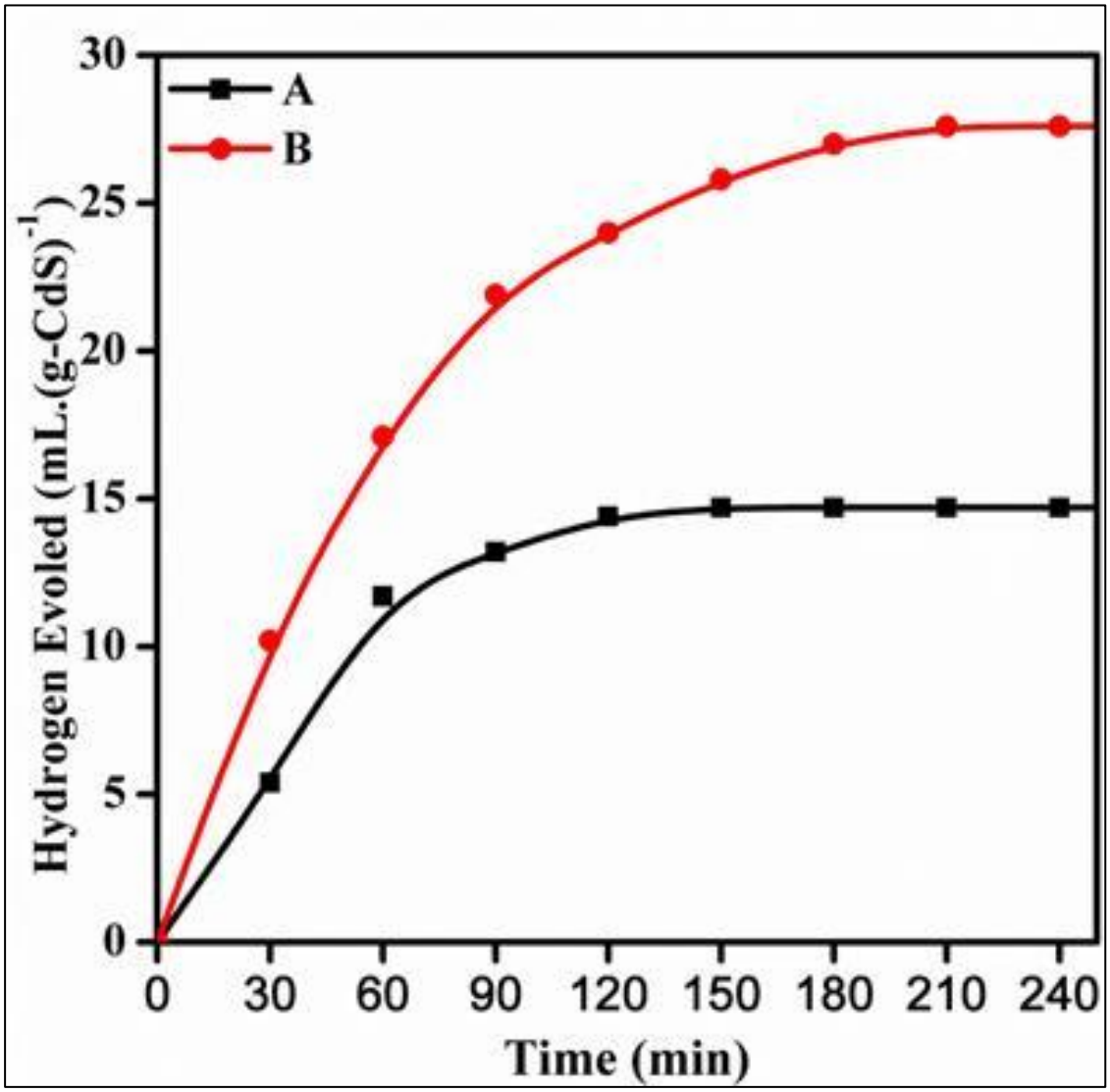


**Figure 4.25:** Hydrogen evolved vs. time with ultrasound (Input power 35 W).

The results of experiment of photocatalytic dissociation of water with ultrasound are shown in Fig. 4.25. It is observed that the total amount of hydrogen produced increased to 24 mL in 2 h when photocatalysis was carried out in presence of ultrasound

in comparison to 14.4 mL when photocatalysis was not combined with ultrasound. Literature reports [Referred section 2.8] that ultrasound may enhance the rate due to:

(a) Formation of reactive intermediates (like $OH^{\cdot}$),

(b) Rise in temperature and thus making thermochemical reaction faster,

(c) Making more surface of catalyst available for a greater absorption of light and

(d) Enhanced transport of intermediate or product from the surface to bulk.

(e) The catalyst cleaning effect and degassing effect.

Several experiments were performed to find out responsible factors for enhancement of hydrogen production. Details are given below.

### 4.10.2 Effect of ultrasonication power

Experiments were carried out with different input energies of ultrasound. The results are shown in Fig. 4.26. When 15W ultrasonic power was applied; hydrogen evolution increased by 5% only. It goes on increasing till an input power of 35 W when the observed increment was 66.6%. No further enhancement in hydrogen production was observed with further increase in ultrasound power beyond 35 W.

It has been reported in literature that when ultrasound was applied in reaction for reactive species (·OH) were formed. Moreover, sonolysis of water alone could also give such type of species. Mead et al. [345] reported that the primary process of sonolysis of water was the formation of H and OH (radicals), as $H_2O \rightarrow \cdot H + \cdot OH$. Suslick et al. [346,347] reported that sonolysis of water in which ultrasound was capable to create extreme temperature and pressure condition resulting generation of free radicals ·H and ·OH), such radicals lead to the formation of $H_2$ and $O_2$ gases. In our case, since no oxygen

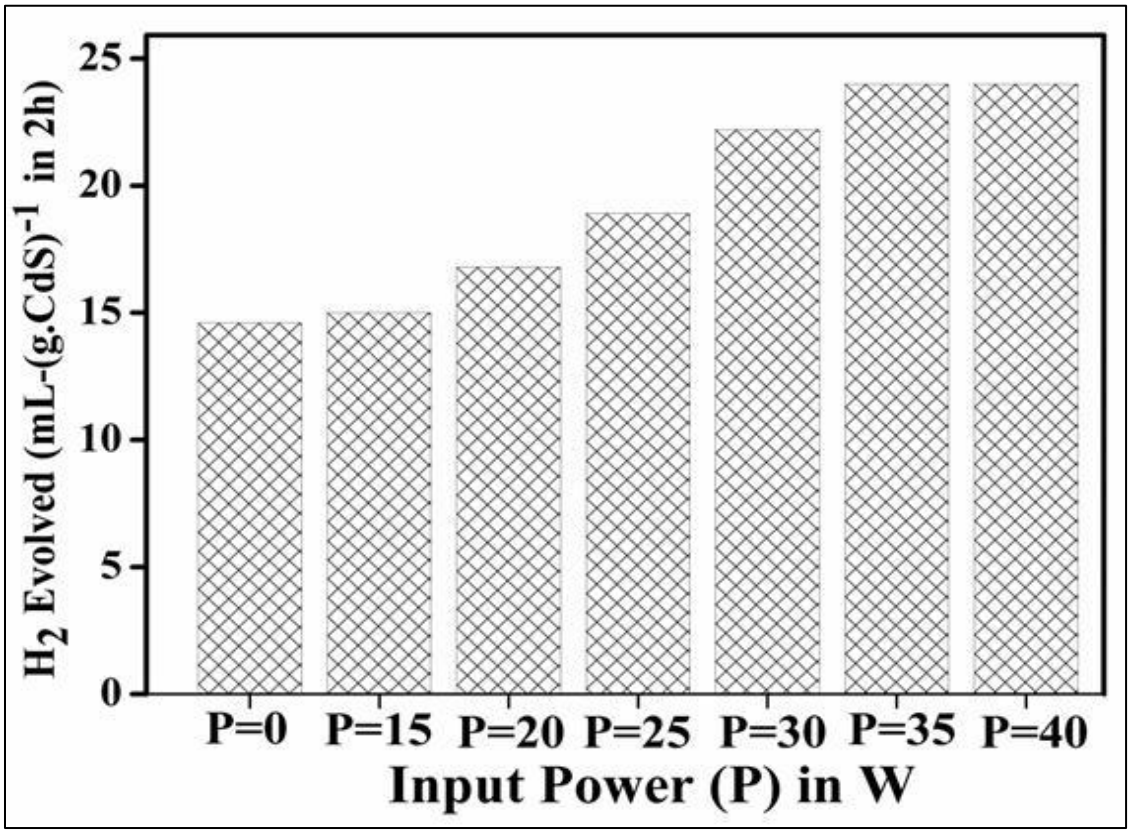


**Figure 4.26:** Hydrogen evolved (in 2 h) vs ultrasonication power applied in photocatalytic reaction with solar radiation.

was detected. Moreover, no enhancement is observed beyond the power of 35 W. Therefore, the formation of radicals cannot be the reason for the observed enhancement in our case. Further, ~200 mesh size catalyst was used in all the experiments and which were well agitated. Therefore, creation of new surface area and a greater absorption of light may not be important. It is observed that beyond a power input of 35 W, there was no enhancement in total hydrogen production. Therefore, a greater absorption of light due to ultrasound may not explain the observed enhanced rate due to ultrasound.

### 4.10.3 Effect of temperature

Effect of rise in temperature due to ultrasound was also investigated. It was observed that when ultrasound was employed during photocatalysis of water, the

temperature of the photoreactor rose from 299 to 318 K. To ascertain the effect of temperature on photocatalysis of water, experiment was carried out maintaining the temperature of reactor at 318 K in the absence of ultrasound. Hydrogen production increased from 14.4 to 15.9 mL.(g-$CdS^{-1}$) in 2 h i.e. an enhancement of ~10%. It means the volume of hydrogen production was ~10% higher than that obtained when the temperature was not maintained constant. It is in order to mention that Sebate et al. [233] have studied the kinetics of photocatalysis of water for hydrogen production from sulphide and sulphite waste streams. They have reported activation energy of 2.52 kcal/mol. Accordingly, a calculation shows that enhancement in rate of production when temperature rises from 299 to 318 K cannot be more than 28%. We have observed ~70% enhancement in the rate of photocatalytic hydrogen production when assisted by ultrasound. Therefore, the observed rate is not primarily due to rise in temperature by ultrasound.

Therefore, on the basis of results of the experiments discussed above, it is concluded that the mechanical energy of the sound wave or those of shock wave created by collapse of bubbles formed due to cavitation were responsible for the increase in the hydrogen production rate. The overall photocatalytic process consists of the following steps:

(a) Absorption of a photon and creation of electron-hole pairs,

(b) Adsorption of reactants on the surface of catalyst,

(c) Reaction on the surface of catalyst,

(d) Desorption of intermediates and (or) products,

(e) Transfer of intermediate and (or) products from surface to bulk of the liquid, and

(f) Subsequent liquid phase reaction.

It is proposed that the mechanical energy of ultrasound has enhanced the transfer of intermediates and products for surface to bulk of liquid. This can be explained by drawing an analogy with boiling phenomenon on a heated plate.

### 4.10.4 Bubble detachment

Drawing an analogy with boiling phenomenon on a heated plate, we studied the possible role of bubble formation and its detachment from the catalyst surface. The forces acting on a bubble on any solid surface which cause detachment of bubble are buoyancy, shear lift and contact pressure forces whereas forces opposing detachment are drag force and force due to surface tension. The forces are depicted in Fig. 4.27 [348]. At a certain critical size of the bubble, the forces causing detachment overcome the forces opposing the same and the bubble gets detached from the surface.

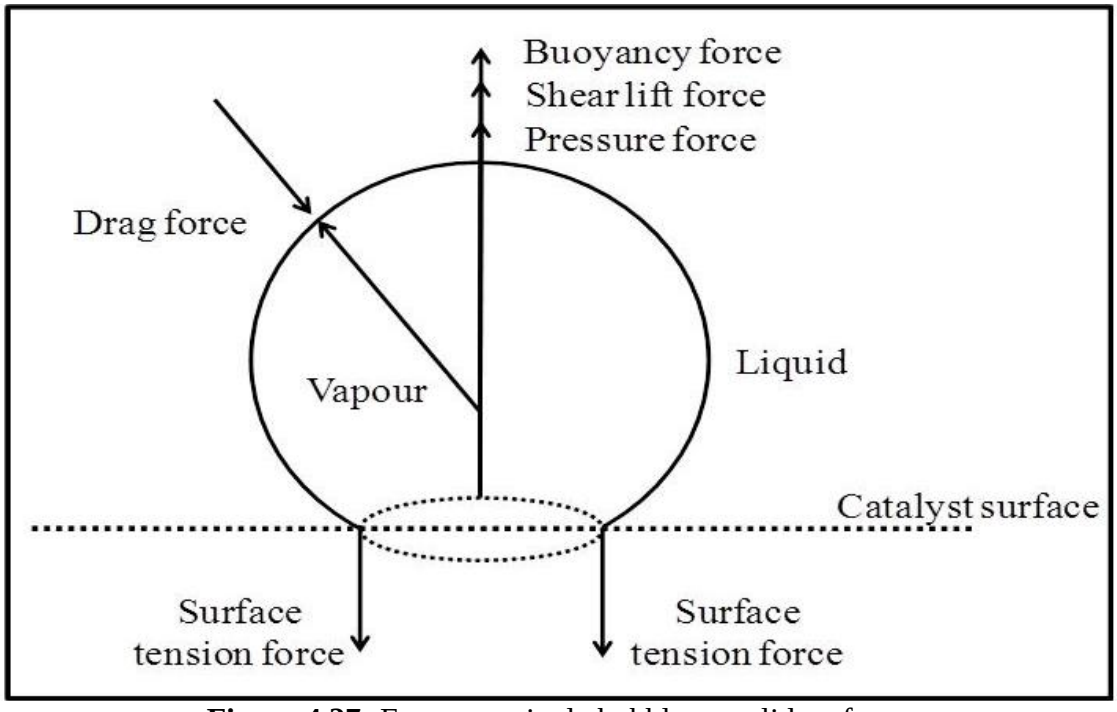


**Figure 4.27:** Forces on single bubble on solid surface.

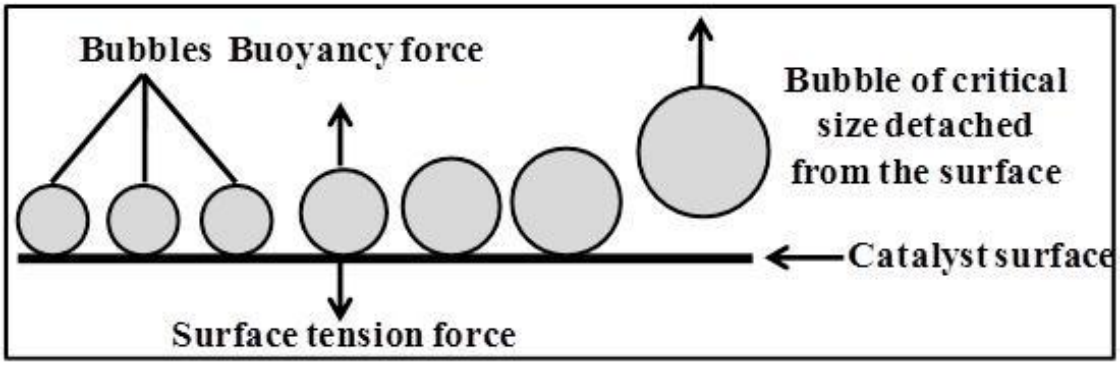


**Figure 4.28:** Schematic representation of hydrogen bubbles on catalyst surface without ultrasound.

Considering only surface tension force and buoyancy force, Fritz [349] developed an equation of bubble departing diameter ($d$):

$$\mathrm{d\ (mm)} = 0.208\theta \left[\frac{\sigma}{g(\rho_L - \rho_g)}\right]^{1/2} \tag{4.9}$$

Where, $\sigma$ is the surface tension, $\theta$ is contact angle, $g$ is gravitational acceleration and $\rho_L$ & $\rho_g$ are density of liquid and gas, respectively.

Similarly, during the photocatalytic reaction the hydrogen gas which is formed on the surface will remain on the surface till its bubble grows to critical size (departing size). A schematic representation of surface of the photocatalyst is shown in Fig 4.28.In such a situation, a fraction of surface of the photocatalyst will remain occupied by hydrogen and thus become unavailable for the adsorption of reactant ($HS^-$). As shown in the Fig. 4.28, the force due to surface tension prevents bubble detachment and critical size of departing bubble in proportional to (surface tension)$^{½}$. Hence, any reduction in surface tension will reduce the critical size of departing bubble and will facilitate detachment of bubble of smaller size and thus providing a larger fraction of catalyst surface for adsorption and reaction with an enhancement in rate.

Since surface tension plays an important role in the bubble detachment, experiments were further carried out to study the effect of surfactant on hydrogen production rate. A sulphur based surfactant (sodium dodecyl sulphate 5 mmol/L) was mixed in the electrolyte solution containing catalyst and hydrogen production was measured for:

(a) Photocatalysis alone, and

(b) Photocatalysis with ultrasound.

A sulphur based surfactant was used because the catalyst was sulphide and electrolyte was also solution of sulphide and sulphite. The results are shown in Fig. 4.29A and 4.29B respectively. It is observed that in the case of photocatalysis alone the amount of hydrogen evolved increases from 14.4 mL to 16.2 mL in 2 h, whereas no such increase was observed in case of photocatalysis with ultrasound. Since a surfactant reduces the surface tension, it has increased the rate of hydrogen production when no ultrasound was used.

The above observations can be explained on the basis of bubble growth and its detachment from the surface. After the desorption of product hydrogen from the active sites of photocatalyst, the hydrogen will remain on the surface of catalyst due to various forces acting on it. Therefore, when the experiment was carried out by adding a surfactant in the liquid, the enhanced hydrogen production rate was observed when the photocatalysis was carried out in absence ultrasound waves.

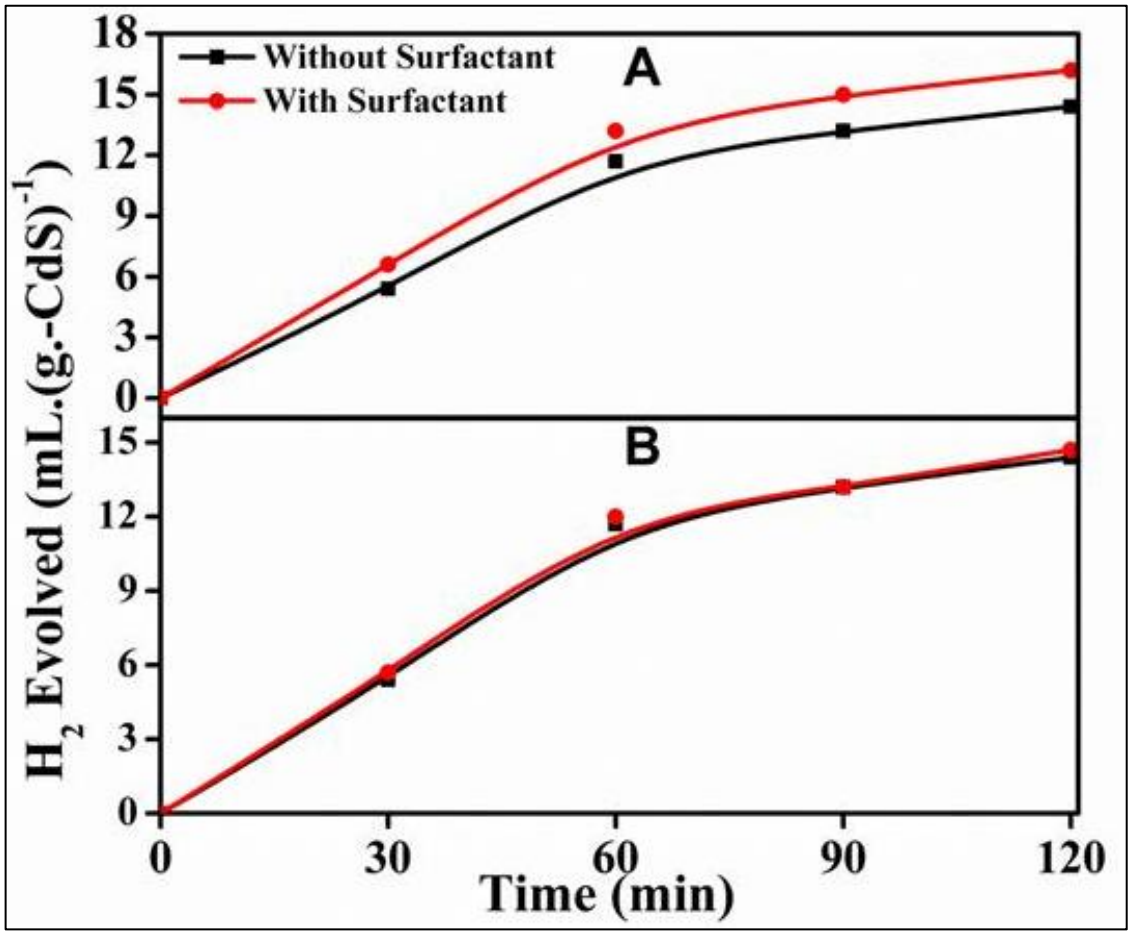


**Figure 4.29:** Effect of surfactant - hydrogen evolved by photocatalysis A: without ultrasound B: with ultrasound.

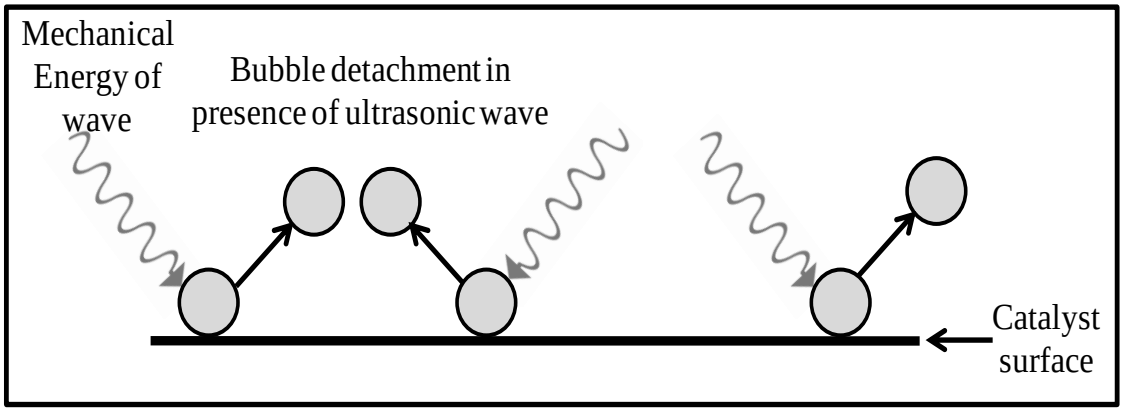


**Figure 4.30:** Schematic representation of hydrogen bubbles on catalyst surface with ultrasound.

However in presence of ultrasound waves, no such enhancement was observed. It is attributed to the fact that the mechanical energy of ultrasound waves destabilizes the bubbles on the surface and bubbles of much smaller sizes are released. A schematic representation of the bubble detachment from the surface of photocatalyst in presence of ultrasound is shown in Fig. 4.30. Therefore, reduction in surface tension did not have [Fig. 4.29] any noticeable effect on bubble departure size and hydrogen production rate when photocatalysis was carried out in the presence of ultrasound.

Thus, the observed increase in the rate of hydrogen production by photocatalysis assisted by ultrasound is due to the faster detachment of bubbles from the surface by overcoming the surface tension force with the help of mechanical energy of ultrasound wave. As reported earlier the rate increased with the increase of input power of ultrasonication but beyond a 35 W power, no further enhancement was observed. It is clear that if bubbles detach as soon as they are formed, the overall process shall be governed by the rate of generation of hydrogen and the effect of ultrasound wave beyond a certain input of power shall not lead to any further enhancement. In addition to the mechanical energy of ultrasound wave, mechanical energy of shock wave due to collapse of bubbles formed by cavitations may also destabilize the hydrogen bubbles on the surface. Thus the higher rate of transfer of hydrogen due to the mechanical energy of ultrasound has been attributed to the enhancement of hydrogen production rate when photocatalysis was carried out in presence of ultrasound.

### 4.11 Kinetics of hydrogen production by dissociation of water

The results of hydrogen production without ultrasound for repeated runs are shown in Fig. 4.31. Hydrogen production rates were also calculated at different duration

by measuring the slopes of curves of Fig. 4.31 and are shown in Fig. 4.32. Before each run the liquid was purged with $N_2$ gas for 1 h. Further at end of any run the light was put off and the liquid with catalyst was kept in dark for more than 6 h and also solution was replenished with requisite amounts of electrolytes (sodium sulphide and sodium sulphite) as calculated by the stoichiometric equation (Eq$^n$. 4.18).

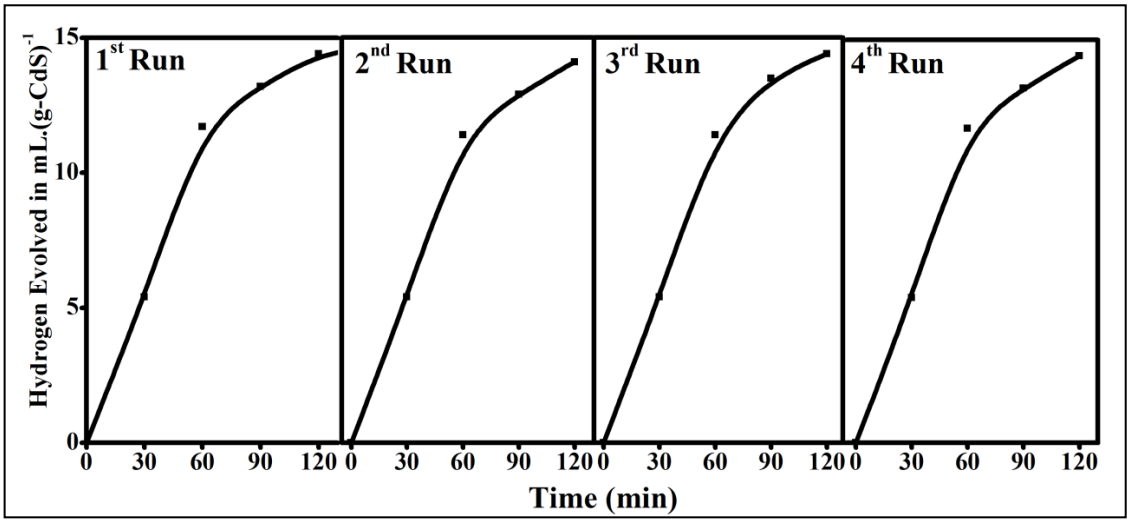


**Figure 4.31:** Hydrogen evolved vs time without ultrasound.

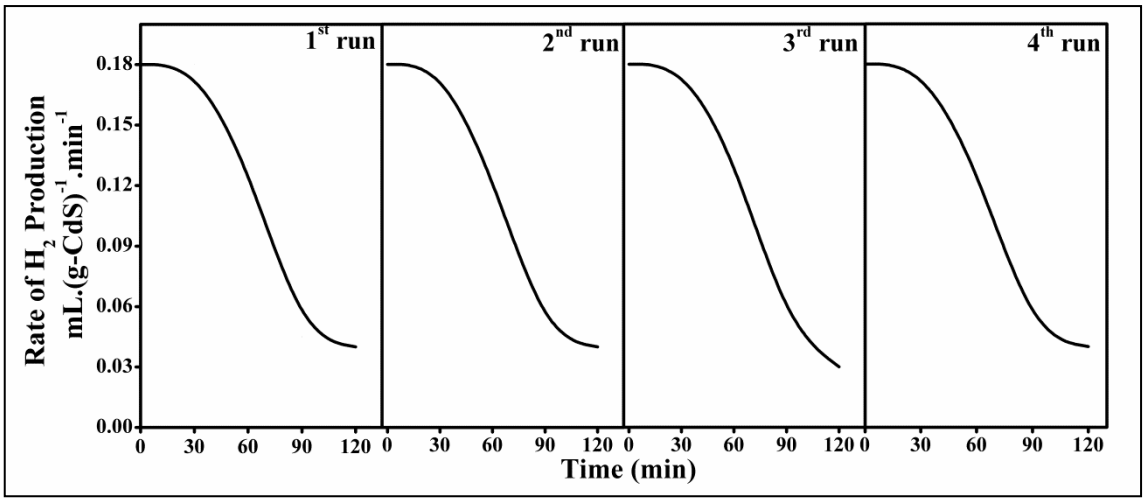


**Figure 4.32:** Hydrogen production rate without ultrasound

It is observed from the Fig. 4.31 that for each run the amount of hydrogen production increased with time initially and gradually it became constant with time, i.e., hydrogen production stopped beyond two hours of irradiation. However, when the light is put off for over six hours and solution was purged, the activity was regained. The same trend was followed for 4 runs.

It is observed from the Fig. 4.32 that with duration of run the hydrogen production rate was constant for initial 30 min and subsequently started falling down and became negligible after 90 min for all the four runs. It is further observed that if the liquid and catalyst are kept in dark for a sufficient long period of time and the liquid is purged with $N_2$ prior to the start of experiment, the hydrogen production rate was fully regained. In an earlier work [230] in our laboratory same observations were reported and it was concluded that the product hydrogen caused the reversible deactivation of catalyst. The mechanism of deactivation was not explained. It should also be noted that the drop in concentration of $S^{2-}$ in each run was of the order of 10%–15% only. Clearly 10%–15% decrease in concentration of $S^{2-}$ may not be attributed to ~90% decreases in hydrogen production rate. Further, polysulphides are known to deactivate CdS but due to presence of sulphite ions in the liquid, the polysulphide which is formed, reacts with sulphite ions and formed thiosulphate [Refer to section 2.7]. In addition, since the deactivation was completely reversible, the possibility of deactivation due to accumulation of polysulphide was ruled out. Therefore, in the present work also, we attribute the decrease in rate to reversible deactivation of catalyst by hydrogen. It has been further observed that the rate of hydrogen production drops down with time in case of photocatalysis with ultrasound also [Fig 4.32]. It was further observed, as stated earlier that this deactivation of catalyst also was completely reversible. It has at strong

chemisorptions of hydrogen on surface which desorbs slowly. Therefore, more experiments were carried out as described below.

Experiments were further carried out where prior to the start of the experiment the electrolyte solution was saturated with hydrogen by purging hydrogen gas in the solution containing catalyst. Result of the experiments is shown in Fig. 4.34. For comparison, the result of experiment when nitrogen gas was purged is also shown in the Fig. 4.34A. Rates were calculated and are plotted as shown in Fig. 4.34B.

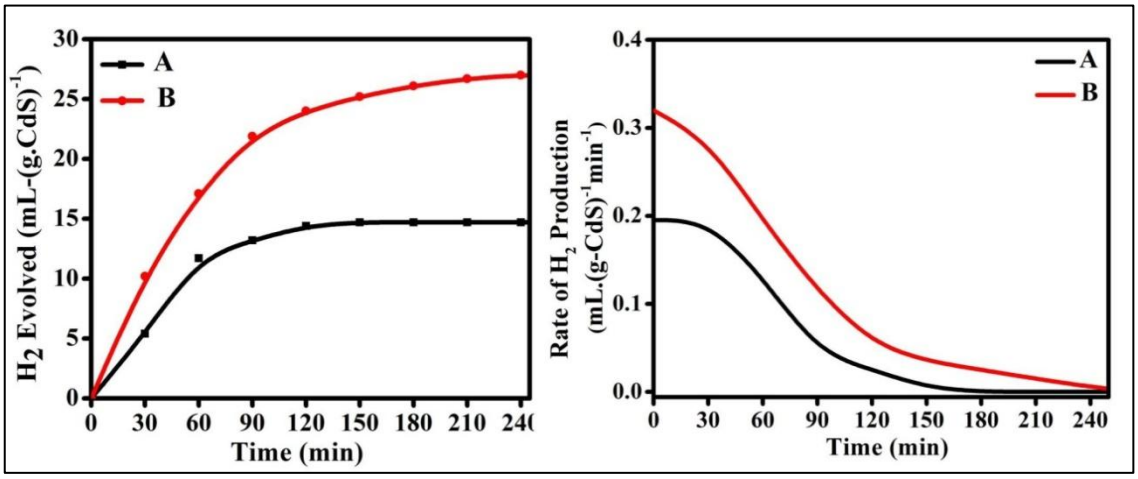


**Figure 4.33:** Hydrogen production rate A: without ultrasound, B: with ultrasound (Input power 35 W).

It is observed that the total hydrogen production as well as rate both have decreased drastically. The total hydrogen production was only 3 mL in 2 h when the liquid was saturated with hydrogen in comparison to 14.4 mL when electrolyte was purged with $N_2$ gas prior to experiment.

Above results clearly show that the presence of hydrogen in the system adversely affects the rate. A similar observation has been reported in literature [235] [Refer to

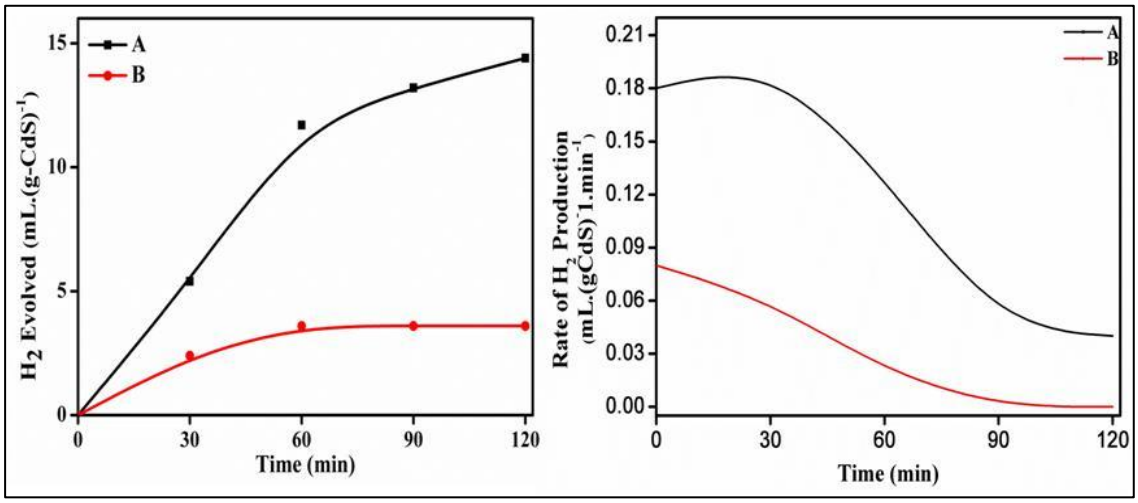


**Figure 4.34:** Hydrogen evolved (without ultrasound) A: electrolyte was purged with $N_2$ for 1 h, B: electrolyte was purged with $H_2$ for 2 h.

section 2.8]. The kinetic steps involved in the dissociation of water will consist of the following steps:

1. Absorption of photon: $CdS + h\upsilon \rightarrow h^+_{CdS} + e^-_{CdS}$ (4.10)

2. Adsorption of reactant on the catalyst surface:

$$H_2O \rightleftharpoons H_2O_{ads} \quad (4.11)$$

$$HS^- \rightleftharpoons HS^-{}_{ads} \quad (4.12)$$

3. Reaction on the catalyst surface:

$$\text{Cathodic: } H_2O_{ads} + 2e^- \rightleftharpoons H_{2_{ads}} + OH^-{}_{ads} \quad (4.13)$$

$$H_{2_{ads}} \rightleftharpoons H_2 \quad (4.14)$$

$$\text{Anodic: } HS^-{}_{ads} + OH^-{}_{ads} + 2h^+{}_{CdS} \rightarrow HS_2^- \quad (4.15)$$

$$HS_2^-{}_{ads} \rightleftharpoons HS_2^- \quad (4.16)$$

4. Raction in the liquid phase: $HS_2^- + SO_3^{2-} \rightarrow S_2O_3^{2-} + HS^-$ (4.17)

5. Global Reaction: $H_2O + HS^- + SO_3^{2-} \rightarrow H_2 + S_2O_3^{2-} + OH^-$ (4.18)

When the desorption of hydrogen (Eq$^{n}$. 4.14) is the rate determining step, its rate of desorption and consequently the overall rate of hydrogen production shall be affected by the presence of hydrogen in the system. Any increase in the concentration of hydrogen will lower the rate of desorption of hydrogen and consequently rate of hydrogen production. Therefore, the decrease in rate of hydrogen production is attributed to gradual built up of hydrogen in the system with time causing decrease in rate of desorption of hydrogen and consequently hydrogen production rate with time. It also explains the observation that hydrogen production rate was fully regained when the system was purged with nitrogen and therefore the deactivation of catalyst was completely reversible. Ultrasound degassing of solution may also be possible leading to a low concentration of hydrogen in solution. In such a case the life of catalyst will prolong which is seen in the Fig. 4.33.

Thus, it may be summarized that the photocatalytic decomposition of water for hydrogen production is affected by both (i) desorption of hydrogen from the active sites and (ii) transfer of hydrogen from the surface of catalyst to the bulk. Ultrasound enhances the rate of transfer of hydrogen from surface to bulk by facilitating the detachment of bubbles from the surface. Therefore, a higher rate of hydrogen production is observed with ultrasound compared to that without ultrasound. However, the rate decreases with time in both cases, i.e. with and without ultrasound. The reason being that rate of desorption (not bubble detachment and transfer) becomes slow with time due to build up of hydrogen in the reaction system. The desorption of hydrogen is adversely affected by the buildup of hydrogen in the reaction system. Since over all kinetics is controlled by the rate determining step which is desorption of hydrogen, the rate was observed to decrease with time.